
ARCHITECTURE DETERMINES OBSERVABILITY IN TRANSFORMERS

Thomas Carmichael

Independent Researcher

ORCID: 0009-0001-3436-1010

github@tdosmail.com

ABSTRACT

Autoregressive transformers make confident errors, but activation monitoring can catch them only if the model preserves an internal signal that output confidence does not expose. This preservation is determined by architecture and training recipe. We define observability as the linear readability of per-token decision quality from frozen mid-layer activations after controlling for max-softmax confidence and activation norm. The correction is essential. Confidence controls absorb 57.7% of raw probe signal on average across 13 models in 6 families.

Observability is not a generic property of transformers. In Pythia’s controlled suite, every tested run with the 24-layer, 16-head configuration collapses to $\rho_{\text{partial}} \approx 0.10$ across a $3.5\times$ parameter gap and two Pile variants, while six other configurations occupy a separated healthy band from 0.21 to 0.38. The output-controlled residual r_{OC} collapses at the same points, and neither tested nonlinear probes nor layer sweeps recover healthy-range signal. Checkpoint dynamics show the collapse is emergent during training. Both configurations at matched hidden dimension form the signal at the earliest measured checkpoint, but training erases it in the (24L, 16H) class while predictive loss continues improving.

Across independent recipes the collapse map changes but the phenomenon persists. QWEN 2.5 and LLAMA differ by $2.9\times$ at matched 3B scale with probe seed distributions that do not overlap, while Mistral 7B preserves observability where LLAMA 3.1 8B collapses despite similar broad architecture. A WikiText-trained observer transfers to downstream QA without training on those tasks, catching errors confidence misses. At 20% flag rate, its exclusive catch rate is 10.9–13.4% of all errors in seven of nine model-task cells. Architecture selection is a monitoring decision.

1 INTRODUCTION

Language models make confident errors that output monitoring does not flag (Guo et al., 2017; Kadavath et al., 2022). The output signals tested here, max softmax probability and trained predictors on the final-layer representation, miss a subset of errors where the model is confident and wrong. A linear probe on frozen mid-layer activations (Alain & Bengio, 2017) reads a different signal: per-token decision quality beyond what output confidence explains. On some architectures, this signal is strong and stable across seeds. On others, no measured layer preserves it in healthy-range, linearly readable form. Figure 1 shows this collapse in two independent training recipes.

Monitorability is an architectural property before it is a monitor-design problem. Most of what probes find in hidden states is output confidence in disguise: on GPT-2 124M, raw Spearman correlation between a linear probe and per-token loss is 0.549, but only 0.282 survives after controlling for max softmax and activation norm. Across 13 models in 6 families, confidence controls absorb on average 57.7% of the raw signal.

The paper makes three claims at different evidential tiers. First, standard probes must control for output confidence: the surviving signal is stable across 20 seeds (± 0.001) and replicates across six families, but raw scores overstate the output-independent component by a factor of two to three; Section 3 establishes this. Second, under Pythia’s controlled training suite, three runs sharing the (24 layers, 16 heads) configuration class collapse to $\rho_{\text{partial}} \approx 0.10$

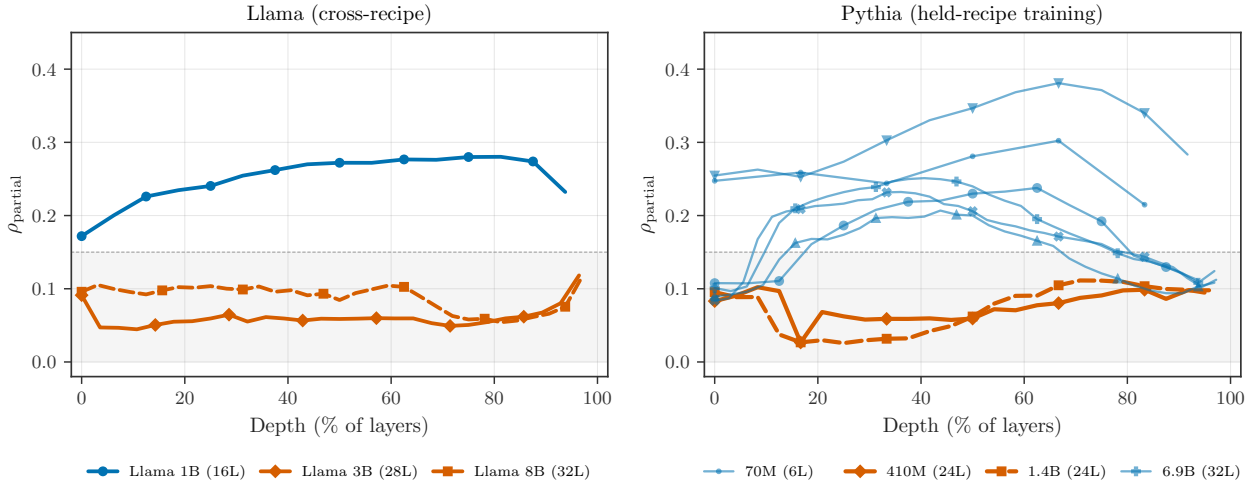


Figure 1: Observability collapse in two training recipes. The y-axis is partial Spearman correlation between a linear probe and per-token loss, after controlling for max softmax probability and activation norm (ρ_{partial} ; Section 2). Left: LLAMA 1B preserves the signal; 3B and 8B do not, under a different training recipe. Right: Pythia configurations outside (24 layers, 16 heads) preserve the signal; the two (24 layers, 16 heads) configurations (410M and 1.4B) collapse under controlled training, replicating across a $3.5\times$ parameter gap with different hidden dimensions (1024 vs 2048). Same protocol, same token budget per hidden dimension. The collapse is discrete, not gradual, and reproduces across recipes.

Table 1: Evidence hierarchy. Each claim is supported at a different evidential tier; the status column reflects the strongest evidence available.

Claim	Evidence	Status
Raw probes are confidence-contaminated	13-model control analysis	Strong
Confidence-independent signal exists	20-seed hardening, shuffle/random tests	Strong
Signal is output-independent	r_{OC} , output-side MLP width sweep	Strong
Configuration determines observability	Pythia controlled suite (3 replications)	Controlled within recipe
Collapse is training-emergent	Pythia 1B vs. 1.4B checkpoint trajectories	Controlled within recipe
Phenomenon generalizes across recipes	Llama/Qwen/Mistral/Phi/Gemma	Observational
Recipe changes the collapse map	Mistral 7B vs. LLAMA 3.1 8B at matched shape	Observational
Operational catch on downstream tasks	LM/SQuAD/MedQA/TruthfulQA	Scoped utility

despite $3.5\times$ variation in parameters and two Pile variants, while six other configurations produce ρ_{partial} between 0.21 and 0.38. The output-controlled residual r_{OC} vanishes at the same collapse points, so what disappears is not a probe metric but the output-independent information the metric isolates. Checkpoint dynamics reveal the mechanism: both matched-width configurations form the signal at the earliest measured checkpoint, but training erases it in the (24L, 16H) class while the healthy configuration recovers (Section 4). Third, cross-family evidence in Section 5 extends the pattern observationally: at matched 3B scale, QWEN 2.5 and LLAMA differ by $2.9\times$ with non-overlapping probe-seed distributions, while Mistral 7B and LLAMA 3.1 8B share broad architecture shape yet diverge. Scale does not predict observability; configuration does. Within a training recipe, configuration is the determining factor. Across recipes, configuration and training dynamics interact at different collapse points. A WikiText-trained observer catches a bounded class of confidence-invisible downstream QA errors without task-specific training. Instruction tuning does not erase observability (Section 5). Architecture selection is a pre-deployment monitoring decision: whether activation-based monitoring can catch a deployed model’s errors depends on the architecture configuration and recipe committed to upstream during training (Table 1).

2 METHOD

Standard probe evaluations mix the quantity we want to measure (decision quality) with output confidence. Our method isolates the residual: a linear probe on frozen transformer activations predicts a confidence-residualized binary target. All models are frozen throughout; only the probe head is trained.

Definition 1 (Observability). *The observability of a transformer at layer l , equivalently its linear readability, is the degree to which a linear probe on $\mathbf{h}^{(l)}$ predicts per-token loss beyond what max softmax probability and activation norm explain. The scalar estimator is ρ_{partial} (partial Spearman correlation controlling for these two covariates); r_{OC} is the residual after additionally controlling for a trained output-layer predictor. “Decision quality” refers to this confidence-residual loss signal, not to a broader notion of reasoning correctness.*

Definition 2 (Observability collapse). *An architectural configuration undergoes observability collapse under a training recipe when ρ_{partial} falls to the detection threshold (Section 3) and the output-controlled residual r_{OC} approaches zero, so that linearly readable decision quality is not preserved at any measured layer.*

Observability measures what a linear readout can extract, not what the model’s own computation uses. The confidence controls test a specific claim: whether the mid-layer signal is independent of the output confidence signal at generation time. A signal that survives partial-correlation controls and output-representation controls is information not recovered by the tested output-side readouts.

Scope and assumptions. We study frozen autoregressive transformers, per-token cross-entropy loss, confidence controls based on max softmax and activation norm, linear mid-layer observers, and output-side MLP controls. This is a deliberately narrow definition of decision-quality observability, not a claim about reasoning correctness or semantic truth. The restriction is the point: if a weak, single-pass linear observer reads a signal that output-side predictors miss, the model preserved monitorable information; if even nonlinear probes and full layer sweeps do not recover it, the architecture did not preserve that signal under this protocol.

Target construction. For each non-padding token position i in the evaluation corpus, we compute per-token cross-entropy loss ℓ_i , max softmax probability $\hat{p}_{\text{max},i}$, and $\|\mathbf{h}_i\|$, the L2 norm of the residual stream at layer l (block output; equivalently the input to layer $l + 1$). An OLS regression $\ell_i \sim \hat{p}_{\text{max},i} + \|\mathbf{h}_i\|$ fitted on the training split produces residuals $\epsilon_i = \ell_i - \hat{\ell}_i$. The binary target is:

$$y_{\text{resid},i} = \mathbf{1}[\epsilon_i > 0]. \quad (1)$$

The target is approximately balanced: OLS residuals are mean-zero by construction and empirically near-symmetric across WikiText-103 tokens. Binary cross-entropy supervision rather than regression on the residual magnitude is a design choice analyzed in Section 3. Because $\|\mathbf{h}_i\|$ is layer-specific, the binary target is constructed separately for each model and layer. Layer profiles therefore measure the readable confidence residual signal at each depth under that layer’s own norm control.

Observer probe. The observer is a linear head on frozen residual stream activations at layer l :

$$o(\mathbf{h}^{(l)}) = \mathbf{w}^\top \mathbf{h}^{(l)} + b. \quad (2)$$

Training uses binary cross-entropy on y_{resid} with Adam (lr = 10^{-3} , batch size 4096, weight decay 10^{-4}) for 20 epochs. The probe has $d + 1$ parameters. No activation function, no hidden layer.

Evaluation: partial correlation. All reported correlations are Spearman rank partial correlations controlling for confounds $\mathbf{c} = [\hat{p}_{\text{max}}, \|\mathbf{h}\|]$. After rank-transforming all variables, we project out the controls:

$$\begin{aligned} \rho_{\text{partial}}(s_\theta, \ell \mid \mathbf{c}) &= \text{corr}(r_{s_\theta|\mathbf{c}}, r_{\ell|\mathbf{c}}) \\ r_{x|\mathbf{c}} &= x - \mathbf{C}(\mathbf{C}^\top \mathbf{C})^{-1} \mathbf{C}^\top x. \end{aligned} \quad (3)$$

Here $s_\theta = o(\mathbf{h}^{(l)})$ is the probe score and \mathbf{C} is the matrix of ranked control covariates with an intercept column. Spearman correlation is invariant to monotone transformations of a scalar score. Logit-level temperature scaling can reorder max-softmax values across examples in multiclass settings, so the nonlinear MLP and logit-entropy controls in Section 3 serve as the empirical robustness check.

Output-controlled residual. An MLP ($d \rightarrow 64 \rightarrow 1$, ReLU) trained on last-layer activations to predict loss $\hat{\ell}_\psi^{(L)}$ is the output-side control. The MLP is trained with Adam (lr = 10^{-3} , batch size 1024, weight decay 10^{-4}) for 20 epochs on the probe’s training split; its predictions on the held-out evaluation tokens form $\hat{\ell}_\psi^{(L)}$:

$$r_{\text{OC}} = \rho_{\text{partial}}\left(s_\theta^{(l)}, \ell \mid \mathbf{c}, \hat{\ell}_\psi^{(L)}\right). \quad (4)$$

Table 2: What each monitoring signal establishes. The output-controlled residual r_{OC} is the only single-signal test of output-independence.

Signal / protocol	Predicts loss	Removes confidence	Tests output independence	Detects collapse
Output confidence	✓			
Raw activation probe	✓			Weakly
ρ_{partial} (conf.-controlled)	✓	✓		✓
r_{OC} (output-controlled)	✓	✓	✓	✓
Nonlinear / layer sweeps	✓	✓	Partly	Artifact
Pythia controlled suite	✓	✓	✓	Controlled (within recipe)

Positive r_{OC} means the mid-layer observer reads information not recovered by the trained final-layer predictor. A width sweep (64 to 512 units) tests whether this result depends on predictor capacity (Section 3). Table 2 maps each monitoring signal to the questions it can answer.

Each level of this hierarchy tests against a different alternative explanation. Confidence control tests whether the probe merely recapitulates output confidence. Output control tests whether the mid-layer signal is merely re-reading information recoverable from the final-layer representation by the tested output-side predictors. Positive r_{OC} means the observer is complementary to those predictors: it reads confidence-independent loss information they do not recover. When r_{OC} collapses together with ρ_{partial} , the complementary, output-independent component is no longer preserved in linearly readable form under this protocol. Under a fixed recipe, this is what it means for architecture to determine observability: it determines whether the output-independent component that activation monitors need survives. We use $\rho_{\text{partial}} \leq 0.15$ as the empirical detection floor because random, shuffled, and underpowered probes cluster near or below this range (Section 3); healthy architectures in adequately powered settings begin at $\rho_{\text{partial}} \geq 0.21$ (exact minimum 0.208, Pythia 2.8B). The gap between these thresholds is treated as an indeterminate margin.

Seed agreement. Seed agreement τ_{seed} is the mean pairwise Spearman correlation of observer scores across k independently initialized probes on the same frozen activations:

$$\tau_{\text{seed}} = \frac{2}{k(k-1)} \sum_{i < j} \rho_s(o_i, o_j). \quad (5)$$

Observed τ_{seed} on frozen activations typically exceeds 0.9, consistent with convergence to a single direction across initializations. Full seed-count analysis in Section 3.

Target validity. We construct the target by residualizing against confidence, then evaluate against the same controls. Five empirical tests address this circularity: (1) hand-designed activation statistics fail under the same target, (2) the probe fails on LLAMA 3B under the identical target, (3) within-domain C4 training fails, (4) random untrained probes produce near-zero ρ_{partial} (one exception: Gemma 3 1B, a geometry artifact), (5) a shuffle test on randomized labels produces near-zero ρ_{partial} . Full results in Section 3.

Evaluation data. All transformer experiments use WikiText-103 (Merity et al., 2017) with the standard train / validation / test splits. We train probes on the train split, select layers on the validation split with seed 42, and report mean ρ_{partial} across 7 held-out validation seeds (43–49) at the fixed layer. A separate test-split evaluation confirms that headline rankings are preserved (Section A). For hardening, 20 additional seeds on GPT-2 124M (Section 3) run at the same fixed layer. The v3 standard token budget is 350 examples per hidden dimension, where an example is one non-padding token position. For downstream tasks, the WikiText-trained probes are applied frozen with no task-specific retraining (Section 5). Because the observer is a linear direction in a d -dimensional residual stream, cross-scale comparisons require token budgets scaled by hidden dimension. On QWEN 2.5 0.5B ($d = 896$), a seven-point sweep from 150 to 1,000 examples per hidden dimension reveals a budget threshold between 450 and 600 examples per hidden dimension: below 450, partial correlation is precise but near the ρ_{partial} detection floor; above 600, the signal rises to the reported healthy value (Section C). Low-budget estimates have low seed variance, so small confidence intervals do not guarantee adequate power. All reported cross-scale comparisons use budgets above each model’s empirically adequate threshold (Gemma 3 1B at 150 ex/dim is adequate for its hidden dimension; see Section C). Collapsed models (LLAMA 3B, 8B;

Table 3: Hand-designed activation statistics on GPT-2 124M (layer 11). All collapse to near-zero partial correlation under confidence controls.

Observer	Partial corr
FF goodness ($\sum h_i^2$)	-0.010
Active ratio	-0.057
Activation entropy	-0.110
Activation norm	-0.002
Learned linear binary	+0.282

Pythia 410M, 1.4B) remain collapsed at absolute token budgets well above the detection regime, so underpowering does not explain collapse. Sensitivity analysis for layer selection in [Section A](#).

Statistical model. Cross-family comparisons use a mixed-effects model with per-seed observations, random intercepts per model (absorbing within-model correlation from shared data and layer selection), and fixed effects for $\log_{10}(\text{params})$ and family:

$$\rho_{\text{partial } ij} \sim \log_{10}(N_i) + \text{family}_i + (1 \mid \text{model}_i). \quad (6)$$

Full specification and variance decomposition in [Section 5](#). Family-level significance is assessed via a Monte Carlo permutation test (50,000 samples) on model-mean ρ_{partial} , with $\log_{10}(\text{params})$ residualized before permutation ([Section 5](#)). [Table 1](#) summarizes the claim hierarchy and the evidence supporting each tier.

3 A CONFIDENCE-INDEPENDENT QUALITY SIGNAL

A confidence-independent quality signal exists in some models, and part of it is output-independent. This section establishes three properties: the signal survives stronger controls than prior probing uses, it survives stress tests of the target construction and nonlinear alternatives, and it localizes at mid-depth with an output-independent component. Existence and hardening results use GPT-2 models ([Radford et al., 2019](#)) (124M–1.5B) on WikiText-103. Cross-model stress tests are noted where they appear. Cross-family replication follows in [Section 5](#).

Hand-designed observers fail. Every hand-designed activation statistic collapses under confidence controls. On GPT-2 124M, FF goodness, active ratio, activation entropy, and activation norm all produce near-zero or negative ρ_{partial} after controlling for confidence and activation norm ([Table 3](#)). Raw correlations are easy to produce; survival under confidence controls is the bar.

The signal survives nonlinear and entropy controls. Beyond max softmax and activation norm, two additional empirical controls do not kill the signal ([Figure 2](#)). A nonlinear MLP trained on $[\hat{p}_{\text{max}}, \|\mathbf{h}\|]$ to predict loss yields $\rho_{\text{partial}} = 0.289$, ruling out nonlinear functions of these two controls as the source of the residual. The nonlinear MLP can represent Platt scaling and other scalar recalibrations of max-softmax confidence as special cases, so the signal is not explained by miscalibrated confidence. Logit entropy as a third control absorbs a further 31% ($\rho_{\text{partial}} = 0.196$), indicating the observer partially reads the shape of the output distribution.

Confidence absorbs most of the raw signal across families. Across 13 models in 6 families, standard controls absorb $57.7\% \pm 12.6\%$ of the raw signal. Half to two-thirds of what probes find in hidden states is output confidence in disguise. Gemma 3 1B is the lone outlier at 21.1%. The other twelve fall in the 48.6–75.8% band (mean $60.8\% \pm 6.5\%$). Full per-model breakdown in [Section A](#).

A learned probe recovers observability. A linear probe trained on the residualized binary target ([Equation \(1\)](#)) recovers $\rho_{\text{partial}} = 0.282 \pm 0.001$ ([Equations \(2\)](#) and [\(3\)](#)) on frozen GPT-2 124M (20 seeds at layer 11, the hardening reference layer) with seed agreement 0.993 ([Equation \(5\)](#)). The standard 7-seed protocol at the peak layer 8 yields 0.290. The MLP-comparison protocol reports 0.293 at its selected layer. The three values span 0.011 under different seed and layer choices, within the ± 0.015 top-three layer flatness ([Section A](#)). Binary supervision produces higher seed agreement than regression because the heads converge on a shared decision boundary ([Section A](#)). Random untrained probes produce near-zero ρ_{partial} on tested architectures. The one elevated baseline (Gemma 3 1B at 0.213) reflects representation geometry rather than decision-quality readability ([Table 6, Section 5](#)).

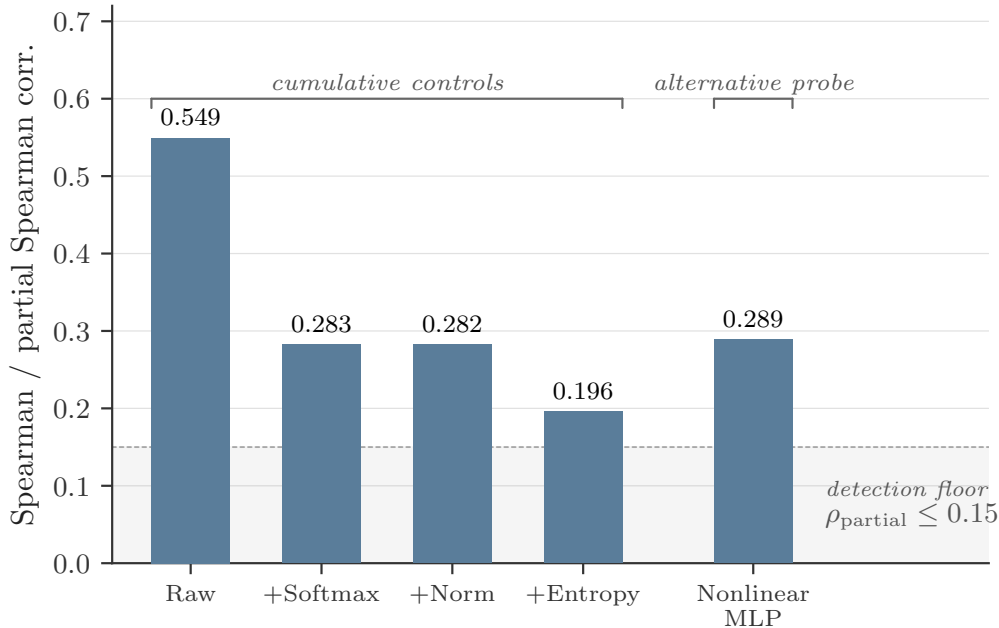


Figure 2: Control sensitivity on GPT-2 124M. The first four bars are cumulative: raw Spearman (0.549), then adding softmax control (0.283), then norm (0.282), then logit entropy (0.196). The fifth bar is an independent nonlinear MLP control (0.289), confirming the residual is not a nonlinear function of max-softmax confidence and activation norm.

With existence established, the remaining question is whether the measurement is valid.

Breaking the circularity. The target construction residualizes against confidence, and the evaluation applies the same controls (Section 2). Five tests address this circularity. First, hand-designed activation statistics produce near-zero ρ_{partial} (ff_goodness -0.010 , activation_norm -0.002), so the target is not trivially recoverable from activation geometry. Second, the observer fails on LLAMA 3.2 3B at 0.091 under the identical target, so the same target can produce very different values on different representations. Third, training the observer on C4 web text (same target construction protocol) fails on QWEN 2.5 7B at $\rho_{\text{partial}} = -0.029$ (Section D). Fourth, random untrained probes produce near-zero ρ_{partial} across architectures tested, with one exception: Gemma 3 1B (0.213), a representation-geometry artifact absent at 4B (family-level values in Table 6). Fifth, a probe trained on shuffled labels yields $\rho_{\text{partial}} = 0.014 \pm 0.019$ across 10 permutations on GPT-2 124M, against a real probe score of 0.292: a $21\times$ ratio and 15.0σ above the shuffle null under a Gaussian approximation.

A nonlinear probe does not exceed the linear probe. Under matched hyperparameters and proper held-out selection, a nonlinear probe does not exceed the linear probe. At matched hyperparameters, a two-layer MLP ($d \rightarrow 64 \rightarrow 1$, ReLU, 50 epochs, same learning rate) achieves equal or lower ρ_{partial} on 6 of 8 models. On GPT-2 124M, the MLP scores 0.252 vs. the linear probe’s 0.293 ($\Delta = -0.042$). Pooled across all 8 models, the MLP is statistically equivalent to the linear probe (TOST $p = 0.025$, mean $\Delta = -0.016$, equivalence margin ± 0.03 chosen as the top-3 layer flatness tolerance reported in Section A, i.e., the ρ_{partial} variation attributable to reasonable layer choice). A linear readout is sufficient under the tested protocols.

Hyperparameter-swept MLPs achieve higher values on every model (0.002 to 0.067), but the advantage scales with model capacity, not signal quality, and the comparison is optimistically biased by model selection on the evaluation set. The linearity result matters most where the signal is weak. On LLAMA 3.2 3B, the linear probe scores 0.089 and a swept-HP MLP with held-out selection (fit on train, HP selected on WikiText validation, reported on WikiText test) scores 0.103. Under matched hyperparameters, MLP and linear probe match within seed noise. A five-layer sweep (L0, L7, L14, L21, L27) confirms the absence at every depth. High observability is absent in LLAMA 3B under both matched and held-out-swept nonlinear protocols.

With validity established, the final question is where the signal lives.

The mid-layer signal is partially output-independent. Observability exists at every GPT-2 124M layer, starting at 0.19 (layer 0) and peaking at layer 8 of 12 ($\rho_{\text{partial}} = 0.290$). The output-side control absorbs about two-thirds of the layer 8 signal, but $r_{\text{OC}} = 0.099 \pm 0.008$ survives (3 seeds; Equation (4)). The observer is not re-reading final-layer information from an earlier layer. It reads something the tested output-side predictors do not recover.

Two sensitivity tests check for measurement artifacts. A width sweep (64, 128, 256, 512 units) on the output-side MLP applied to QWEN 2.5 7B absorbs the same ~ 0.10 of raw signal at every width, leaving the OC residual near 0.129 (64-unit) and 0.130 (512-unit). Capacity is not the bottleneck: the 512-unit predictor is statistically indistinguishable from the 64-unit across 3 seeds. A 30-resample document-level bootstrap on QWEN 2.5 7B yields $\rho_{\text{partial}} = 0.238$ (95% CI [0.215, 0.270]), stable under data resampling. Layer 8 carries quality information not recovered by the tested output-side predictors.

SAE features are less aligned than raw activations. Sparse autoencoders (Bricken et al., 2023) decompose activations into interpretable features under a reconstruction objective. A 24,576-feature reconstruction-trained SAE probe (0.255) underperforms the raw linear observer (0.290) despite $32\times$ more input dimensions, with rank correlation 0.70 between the two. Under this SAE, the quality signal is not concentrated in the reconstructed feature basis. It is distributed across the residual stream in a direction the reconstruction-trained decomposition partially obscures. The observer direction is nearly orthogonal to dominant representation variance (PC1 cosine 0.002, top 10 PCs capture 3.7%; Section A); the quality signal occupies a low-variance subspace that variance-dominant and reconstruction-trained decompositions can partially obscure.

The signal scales within GPT-2. Within GPT-2 (124M, 355M, 774M, 1.5B), the family provides a four-point scaling test with no confounders: same architectural template, tokenizer, and training distribution. Partial correlation is stable across $12\times$ scale (0.279 to 0.290; bootstrap 95% CIs overlap). What changes is not the total signal but how much of it the output layer retains: r_{OC} grows monotonically from 0.099 to 0.174. Larger models carry more quality information that their output layers discard. Full per-model breakdown in Section A.

The signal exists and survives artifact tests on GPT-2. Whether all architectures preserve it is the question the next section answers.

4 ARCHITECTURE CONFIGURATION DETERMINES OBSERVABILITY

Pythia is the controlled test. Holding the training suite constant (shared corpus, tokenizer, optimizer family, and schedule template), every tested run sharing the (24 layers, 16 heads) configuration class collapses to $\rho_{\text{partial}} \approx 0.10$, while six other configurations occupy a separated healthy band (0.21 to 0.38) with no intermediate values. We refer to this discrete loss as *observability collapse*. Pythia 1B rules out the parameter-size band; the deduplicated-Pile run rules out the corpus variant; layer sweeps rule out layer-selection artifacts; nonlinear probes rule out linear-readout limitations; r_{OC} collapse rules out output-redundancy under the tested output-side predictors as an explanation. Checkpoint dynamics show the signal forms and strengthens early in both matched-width configurations, then training erases it in the (24L, 16H) class while the healthy configuration recovers. Within this controlled suite, the remaining supported explanation is architecture configuration.

The Pythia suite (Biderman et al., 2023) holds corpus, tokenizer, optimizer family, and schedule template constant across eight sizes from 70M to 12B; learning rate and batch size scale with model size while architecture varies. The three (24 layers, 16 heads) collapse points are Pythia 410M (0.105), Pythia 1.4B (0.106), and Pythia 1.4B-deduped (0.100, same architecture as 1.4B but trained on the deduplicated Pile (Gao et al., 2021) variant), each measured across 7 probe seeds. The three agree to within a 0.006 total range despite $3.5\times$ variation in parameters, $2\times$ in hidden dimension, $2\times$ in head dimension, and two Pile variants. At 410M the seed variance is ± 0.0009 , the tightest measurement in the paper.

Six other Pythia configurations, spanning depths 6 to 36 and head counts 8 to 40, produce ρ_{partial} between 0.21 and 0.38. Pythia 1B (16 layers, 8 heads, 0.246) sits between the two collapsed models in parameter count but produces healthy observability, ruling out the 400M–1.5B size band as the collapse trigger. The collapse is tied to the (24, 16) configuration class, not to scale.

The right panel of Figure 1 shows layer-wise profiles for all eight Pythia sizes: six configurations peak at mid-to-late depth between 0.21 and 0.38, while the two (24 layers, 16 heads) configurations (410M and 1.4B) stay flat near 0.10

Table 4: Pythia suite under held-recipe training (The Pile, same tokenizer, same optimizer family). Three runs sharing the (24 layers, 16 heads) configuration class collapse (bold), replicated across a $3.5\times$ parameter gap (410M vs. 1.4B), $2\times$ hidden dimension and $2\times$ head dimension, and two Pile variants (regular vs. deduplicated at 1.4B). Six other configurations produce ρ_{partial} between $+0.21$ and $+0.38$. The output-controlled residual r_{OC} collapses at the same three runs ($\leq +0.05$, including negative), while healthy configurations range $+0.09$ to $+0.17$. All values are 7-seed means on held-out seeds 43–49 (layer selected via seed 42). Standard deviations are across seeds.

Model	Layers	Heads	Hidden	Head_dim	ρ_{partial}	Seed std	r_{OC}
Pythia-70M	6	8	512	64	0.301	0.001	0.147
Pythia-160M	12	12	768	64	0.382	0.004	0.169
Pythia-410M	24	16	1024	64	0.105	0.001	0.043
Pythia-1B	16	8	2048	256	0.246	0.012	0.120
Pythia-1.4B	24	16	2048	128	0.106	0.006	0.003
Pythia-1.4B-deduped	24	16	2048	128	0.100	0.007	-0.012
Pythia-2.8B	32	32	2560	80	0.208	0.007	0.088
Pythia-6.9B	32	32	4096	128	0.240	0.012	0.110
Pythia-12B	36	40	5120	128	0.238	0.005	0.097

across every depth. The deduplicated 1.4B replication confirms the same pattern (Table 4). At the final checkpoint, the collapsed configurations show no mid-layer peak. The measured residual-stream states show no layer at which healthy-range observability remains. The left panel shows LLAMA under a different training recipe, reproducing the same within-family discontinuity at a different configuration (1B healthy at 16L/32H; 3B and 8B collapse at 28L/24H and 32L/32H).

No single architectural axis predicts the collapse. Collapse is not a monotonic function of any single architectural axis. Deeper models do not collapse harder: 32-layer Pythia (2.8B at 0.208, 6.9B at 0.240) and 36-layer Pythia (12B at 0.238) produce healthy signal. Higher head counts do not collapse harder: 32-head and 40-head configurations are healthy. Depth and head count co-occur at both collapse points (depth=24 AND heads=16) and no other Pythia size matches either value. The two axes are perfectly confounded within this suite.

Baselines and validity. Pythia 70M’s random untrained probe produces 0.078, elevated relative to larger Pythia sizes but still $3.9\times$ below the learned probe’s 0.301. The finding holds with this elevated baseline. Target validity tests carry across to the Pythia setting: the probe training protocol is identical to Section 3, residualizing against the same confidence controls.

Three controlled comparisons, one outcome. The three replications above are three controlled comparisons that each hold the (24 layers, 16 heads) configuration class constant and vary other factors. Varying width, head dimension, and parameter count within the same configuration class (Pythia 410M vs. 1.4B) does not recover observability. Switching from regular to deduplicated Pile at matched architecture (Pythia 1.4B regular vs. 1.4B-deduped) does not recover it. Varying configuration at held training (other Pythia sizes) produces the full range of observability values between 0.21 and 0.38 (Figure 3). The collapse is not an artifact of training data, scale, or probe initialization. Two Pile variants, two sizes with a $3.5\times$ parameter gap, and three 7-seed runs each produce $\rho_{\text{partial}} \approx 0.10$.

Within-Pythia statistical test. If you were allowed to label any two Pythia configurations as collapsed, the actual architecture label, (24 layers, 16 heads), produces the largest gap. An exact permutation test formalizes this: under the null (arbitrary 2-vs-6 partitions), the observed gap of 0.163 is the unique maximum of the $\binom{8}{2} = 28$ possible partitions, giving $p = 0.036$. A one-way F-test on the same split yields $F(1, 6) = 12.03$, $p = 0.013$, with $\eta^2 = 0.667$ (configuration explains 67% of within-Pythia variance). Including the 1.4B-deduped replication as a third collapsed point ($n = 9$, 3-vs-6 split) lowers the permutation p -value to 0.012 (1/84). Leave-one-configuration-out preserves the separation (max collapsed < min healthy) on every removal.

The collapse is signal, not probe failure. A shuffle test at the collapse configuration confirms the residual value is real signal, not a silent probe artifact. Training the same linear probe at layer 17 of Pythia 1.4B (the learned probe’s peak layer at this configuration) on randomly permuted binary labels across 10 permutations yields $\rho_{\text{partial}} = -0.002 \pm 0.036$, scattered symmetrically around zero (per-permutation range -0.059 to 0.051). The real probe’s 0.106 exceeds every one of the 10 shuffled permutations (maximum 0.051); this exceedance is the primary test. A Gaussian approximation

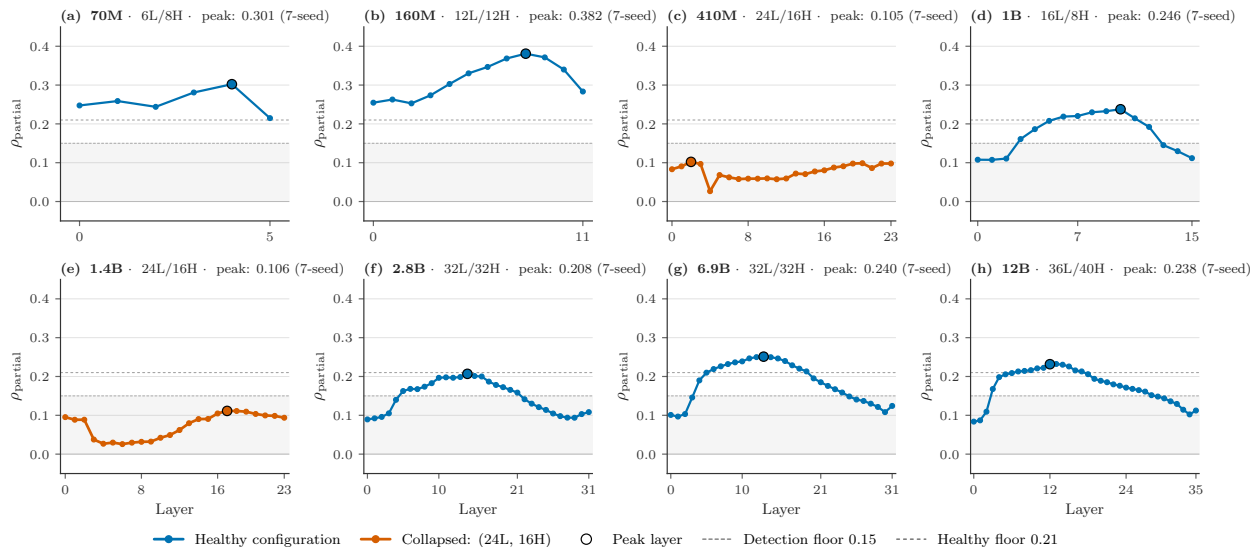


Figure 3: Pythia layer profiles under controlled training. Six healthy configurations peak at mid-to-late depth; two collapse configurations stay flat across all layers. No layer choice rescues the collapse.

of the 10-permutation null gives $z = 3.0$ (sample std, $\text{ddof}=1$); with $n = 10$ the empirical exceedance carries the claim. A code-path sanity check confirms the two pipelines measure the same quantity within 0.002 (Section A). At GPT-2 124M the same protocol produced shuffled 0.014 ± 0.019 against a real 0.292. Pythia 1.4B has wider shuffle variance, but the conclusion holds: shuffled labels yield zero-centered noise; real labels yield measurable signal.

Linear probe is not the bottleneck. A two-layer MLP probe with held-out hyperparameter selection does not close the gap at the collapse points: at Pythia 410M, Pythia 1.4B, and LLAMA 3B, the swept MLP lifts ρ_{partial} but never crosses the 0.21 healthy-band floor (Table 5). Across all three collapse configurations under two training recipes and at two layer choices for LLAMA 3B, the best-achievable nonlinear probe never crosses the healthy floor of 0.21. Probe expressive capacity is not the bottleneck. The collapse reflects a representational property rather than a limit of linear probing.

Table 5: Swept-hyperparameter nonlinear probe with held-out selection (fit on train, select HP on WikiText validation, report on WikiText test). Grid: hidden $\in \{64, 128\}$, lr $\in \{0.01, 0.001, 0.0001\}$, epochs $\in \{20, 50\}$. Δ is swept-HP MLP minus linear on test. Healthy configurations gain $\leq +0.07$ on test and remain in the healthy band (all $\geq +0.21$). The three collapse configurations, tested under two training recipes (Pythia held-recipe; Llama production) and at two layer choices for LLAMA 3B, gain $+0.014$ to $+0.043$ on test and all remain within the collapsed band ($\leq +0.18$), well below the healthy floor. No tested probe recovers healthy-range signal where the linear probe fails.

Configuration	Peak layer	Linear test	Swept-HP MLP test	Δ
<i>Healthy configurations</i>				
GPT-2 124M	L8	0.293	0.339	0.046
QWEN 2.5 0.5B	L19	0.219	0.254	0.035
QWEN 2.5 1.5B	L19	0.277	0.325	0.048
QWEN 2.5 3B	L25	0.286	0.325	0.038
QWEN 2.5 7B	L17	0.244	0.295	0.051
QWEN 2.5 14B	L30	0.228	0.296	0.067
Gemma 3 1B	L1	0.266	0.268	0.002
<i>Collapsed configurations</i>				
LLAMA 3.2 3B	L0	0.088	0.102	0.014
LLAMA 3.2 3B (layer check)	L27	0.104	0.147	0.043
Pythia 410M (24L, 16H)	L2	0.126	0.139	0.014
Pythia 1.4B (24L, 16H)	L17	0.129	0.172	0.043

Each alternative explanation for the collapse leaves a loophole that the data closes. All tested probes are single-layer. Signal could be confidence leakage, but confidence controls are applied throughout. It could be a linear-readout limitation, but tested nonlinear probes do not cross the healthy floor. It could be layer misselection, but collapsed models show no healthy-range layer at any depth. It could be underpowering, but collapsed models remain collapsed at token budgets well above the budget threshold. It could be architectural incapability, but both configurations form and strengthen the signal early in training. What remains is whether the mid-layer signal is merely redundant with the output representation. That is the test r_{OC} performs.

Output-independence collapses at the same configurations. The output-controlled residual r_{OC} tracks ρ_{partial} across the Pythia suite and collapses at the same three runs (Table 4). Healthy configurations produce r_{OC} between 0.088 (Pythia 2.8B) and 0.169 (Pythia 160M). The three (24 layers, 16 heads) runs produce 0.043 (410M), 0.003 (1.4B), and -0.012 (1.4B-deduped): near-zero or negative output-independent component at each collapse point. Separation is wider on r_{OC} than on ρ_{partial} because collapsed r_{OC} values reach zero or negative. Not only does the confidence-controlled signal vanish at the (24 layers, 16 heads) configuration, but the mid-layer information not recovered by the tested output-side predictors vanishes with it. Architecture configuration determines output-independence, not just partial correlation. Under controlled training, observability collapses discretely at specific architecture configurations, and what collapses is not merely a metric but the output-independent, linearly readable information the metric isolates. The cross-family generalization of this property, across all 25 models measured in the paper, appears in Figure 4: architectures that lose confidence-controlled observability also lose output-independence.

Observability collapse emerges during training. Both matched-width configurations form and strengthen the quality signal early in training. We evaluate two Pythia configurations with matched hidden dimension ($d = 2048$) at 10 checkpoints from step 256 ($\approx 0.5\text{B}$ tokens) to step 143,000 ($\approx 300\text{B}$ tokens). At the earliest measured checkpoint, both the healthy 1B (16L/8H) and the collapsed-at-convergence 1.4B (24L/16H) are in the healthy range: $\rho_{\text{partial}} = 0.315$ and 0.297 respectively, with positive output-controlled residuals ($r_{OC} = 0.079$ and 0.065). By step 1,000 ($\approx 2\text{B}$ tokens), the 1.4B configuration has strengthened further ($\rho_{\text{partial}} = 0.314$, $r_{OC} = 0.113$). The (24L, 16H) architecture is capable of representing the output-independent quality signal early in training. For each checkpoint, losses, confidence controls, residual targets, probe heads, and output-side controls are recomputed using the same protocol as the final-checkpoint experiments.

The trajectories diverge during mid-training (Figure 5). Both configurations experience a drop in ρ_{partial} below the detection floor around step 16,000. The 1B configuration recovers by step 32,000 and, despite late-training variability, converges healthy ($\rho_{\text{partial}} = 0.246$, $r_{OC} = 0.120$). The 1.4B configuration does not: after a transient recovery to the healthy band at step 64,000, it converges to $\rho_{\text{partial}} = 0.106$ and $r_{OC} = 0.003$, matching the final-checkpoint collapse in Table 4. The erasure is selective: the output-independent fraction ($r_{OC}/\rho_{\text{partial}}$) drops from 36% at step 1,000 to 3% at convergence in the 1.4B, while it grows from 33% to 49% in the 1B (Table 12). Perplexity declines monotonically in both configurations through the observability dip, so the quality signal is destroyed while predictive capability improves normally. Architecture determines observability not by preventing the signal from appearing, but by determining whether training preserves or erases it.

Under controlled training, configuration determines whether the signal survives. Whether independent training recipes produce the same phenomenon at different collapse points is the question Section 5 answers.

5 CROSS-FAMILY EXTENSION

Section 4 established that architecture configuration determines whether training preserves observability, with the (24 layers, 16 heads) class forming the signal early but failing to maintain it through convergence. This section extends the test across independent training recipes and characterizes the operational consequences of the architecture effect (Figure 6). Under identical evaluation with token budgets scaled by hidden dimension, five additional families, QWEN 2.5 (Yang et al., 2024), LLAMA (Grattafiori et al., 2024), Gemma 3 (Gemma Team, 2025), Mistral (Jiang et al., 2023), and Phi-3 (Abdin et al., 2024), split into above-floor and collapsed groups. Under the same evaluation protocol, architecture-recipe choice is what differs. These comparisons are observational. The controlled causal test is Pythia (Section 4).

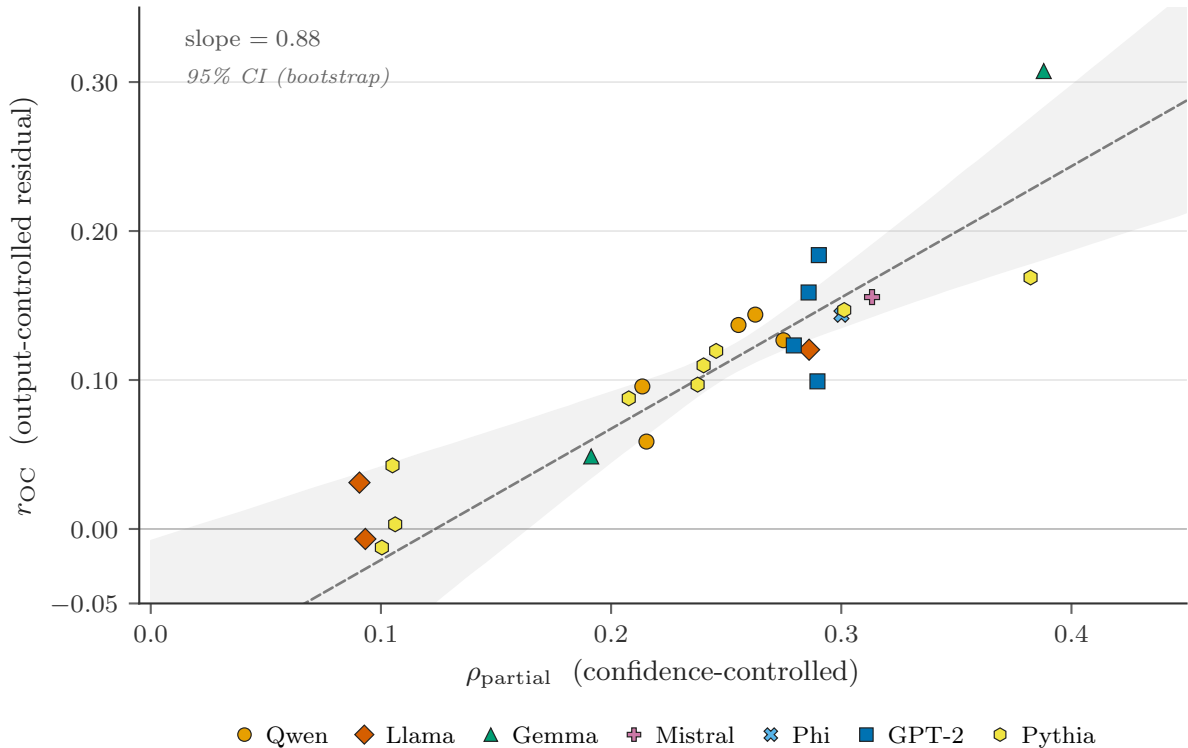


Figure 4: Output-independence collapses with observability. Output-controlled residual (r_{OC}) vs confidence-controlled partial correlation (ρ_{partial}) across 25 models (16 cross-family plus 9 Pythia). Healthy configurations fall on a linear trend (dashed line, slope 0.88). Five collapsed configurations (Llama 3B/8B; Pythia (24 layers, 16 heads), 3 replications) fall near the origin on both axes, off the trend. Architecture-dependent observability and output-independence are two views of the same collapse phenomenon.

Table 6: Observability across six architecture families under identical evaluation protocol. Token budgets scaled by hidden dimension (350 ex/dim, 600 for QWEN 2.5 0.5B). LLAMA 1B matches high-observability families; 3B and 8B drop to near the detection floor.

Model	Family	Params	Peak layer	$\rho_{\text{partial}}^a \pm \text{std}$	r_{OC}	τ_{seed}	Rand. head
QWEN 2.5 0.5B	Qwen	0.5B	L19 (79%)	0.215 0.020	0.059	0.959	-0.055
Gemma 3 1B	Gemma	1B	L1 (4%)	0.388 0.004	0.307	0.980	0.213
LLAMA 3.2 1B	Llama	1.2B	L13 (81%)	0.286 0.006	0.120	0.995	0.012
QWEN 2.5 1.5B	Qwen	1.5B	L18 (64%)	0.275 0.032	0.127	0.953	-0.051
GPT-2 XL	GPT-2	1.5B	L34 (71%)	0.290 0.004	0.174	0.952	—
QWEN 2.5 3B	Qwen	3B	L25 (69%)	0.263 0.021	0.144	0.925	0.023
LLAMA 3.2 3B	Llama	3B	L0 (0%)	0.091 0.006	0.031	0.998	-0.002
Phi-3 Mini	Phi	3.8B	L17 (53%)	0.300 0.002	0.144	0.958	-0.008
Gemma 3 4B	Gemma	4.3B	L6 (18%)	0.191 0.007	0.059	0.802	-0.010
Mistral 7B	Mistral	7B	L22 (69%)	0.313 0.001	0.156	0.995	0.014
QWEN 2.5 7B	Qwen	7B	L17 (61%)	0.255 0.019	0.137	0.964	—
LLAMA 3.1 8B	Llama	8B	L1 (3%)	0.093 0.012	-0.002	0.994	0.005
QWEN 2.5 14B	Qwen	14B	L30 (62%)	0.214 0.032	0.096	0.851	0.009

^a Validation split (held-out seeds, $n = 7$ except GPT-2 XL at $n = 3$). Test split preserves rankings; mean absolute gap 5.2% (Section A).

Gemma 3 1B random head +0.213 reflects representation geometry (absent at 4B). Gemma 3 1B uses 150 ex/dim rather than the standard 350; see Section C.

LLAMA 3B/8B peak at L0/L1: no layer exceeds +0.12; reported peak is argmax of a flat profile.

Qwen preserves observability from 0.5B to 14B. QWEN 2.5 preserves observability across a $28\times$ parameter range (Table 6). Partial correlation stays between 0.21 and 0.28 from 0.5B through 14B. Instruction-tuned variants match or exceed their base counterparts at every scale except 1.5B, where the decrease is -0.009 . The output-controlled residual

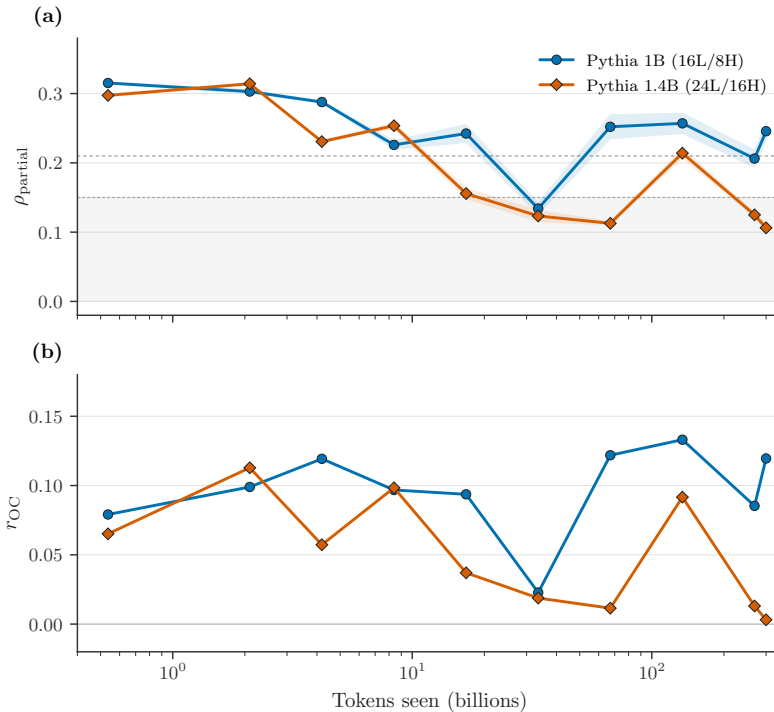


Figure 5: Observability collapse is training-emergent. Both configurations begin with healthy ρ_{partial} at the earliest measured checkpoint. Both dip during mid-training. The (16L, 8H) configuration recovers and converges healthy; the (24L, 16H) configuration converges collapsed. Final perplexities are comparable (18–21), so the divergence is monitorability, not predictive capability. Dashed lines in panel (a): detection floor (0.15) and healthy floor (0.21).

Table 7: Base vs. instruct across QWEN 2.5 scales plus Mistral 7B. Instruction tuning preserves observability; changes are small relative to the cross-family spread.

Scale	Base ρ_{partial}	Instruct ρ_{partial}	Δ
QWEN 2.5 0.5B	0.215	0.312	0.097
QWEN 2.5 1.5B	0.275	0.266	-0.009
QWEN 2.5 3B	0.263	0.265	0.002
QWEN 2.5 7B	0.255	0.291	0.035
QWEN 2.5 14B	0.214	0.237	0.023
Mistral 7B	0.313	0.339	0.026

r_{OC} remains positive throughout, confirming that the signal is not reducible to output-layer information at any scale tested.

Instruction tuning preserves observability. The pattern holds at every QWEN 2.5 scale tested (Table 7):

At 0.5B, instruction tuning increases the signal by $\Delta = 0.097$. At 1.5B through 14B, the delta is small (-0.009 to 0.035). The pattern extends beyond QWEN 2.5: LLAMA 3.2 1B Instruct produces 0.285 versus base 0.286 ($\Delta = -0.001$); Mistral 7B Instruct gives 0.339 against base 0.313 ($\Delta = 0.026$). Whatever produces observability runs deeper than what instruction tuning modifies.

Cross-family divergence separates into two groups. At matched 3B scale, the difference is not subtle: QWEN 2.5 retains strong observability (0.263) while LLAMA sits near the detection floor (0.091), a $2.9\times$ gap. The per-probe-seed distributions do not overlap: every QWEN 2.5 seed (0.225 to 0.288) exceeds every LLAMA seed (0.084 to 0.102). The gap survives nonlinear confidence controls: under the nonlinear MLP on $[\hat{p}_{\text{max}}, \|\mathbf{h}\|]$ (Section 3), LLAMA 3B falls to -0.005 .

GPT-2 (124M–1.5B), Mistral 7B (0.313), and Phi-3 Mini (0.300) confirm strong signal in three additional families. Gemma 3 1B shows the strongest raw signal in the cross-family set (0.388), but this is a representation-geometry artifact

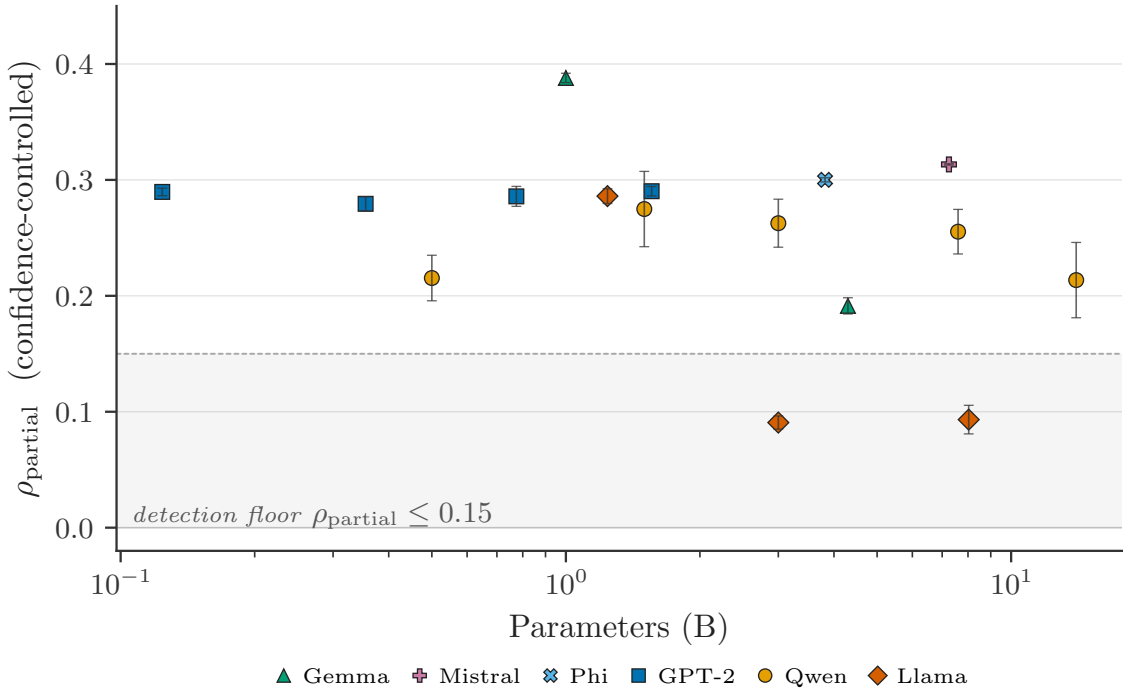


Figure 6: Observability across six families. LLAMA (red) drops from 0.286 at 1B to 0.091 at 3B. Non-LLAMA families remain above the detection floor. Shaded band: detection floor.

rather than stronger observability: a random untrained probe on the same Gemma 3 1B activations already achieves 0.213. At 4B the anomaly disappears (0.191, random baseline -0.010); the anomaly is specific to the 1B configuration (Table 6).

The Llama cliff. The signal does not degrade gradually within LLAMA. It falls from the high-observability group to near the detection floor in a single step (Figure 1, left). The 1B model produces $\rho_{\text{partial}} = 0.286$ under the full 7-seed protocol, matching GPT-2 and the upper QWEN 2.5 range. The 3B model produces 0.091. LLAMA 3.1 8B confirms at 0.093 (7-seed, full protocol), consistent with the 3B result. The architectural configuration changes between 1B and 3B: 1B has 16 layers, 32 heads, and 2048 hidden dimension; 3B has 28 layers, 24 heads, and 3072 hidden dimension. LLAMA 3.2 1B and 3B both use the LLAMA 3.2 pruning/distillation recipe (Meta, 2024) but with different larger-model logit sources (3.1 8B and 70B respectively). The 1B-vs-3B comparison varies architecture and distillation provenance, while the 3B-vs-8B extension crosses the 3.2/3.1 recipe boundary. The cliff reproduces observability collapse at a different configuration (Pythia: 24 layers, 16 heads; LLAMA: 28 layers, 24 heads). Within-family discontinuity is a general architectural phenomenon; which specific configuration collapses is recipe-dependent.

Training recipe changes the collapse map. Mistral 7B and LLAMA 3.1 8B share architectural structure (32 layers, 32 heads, hidden dimension 4096) yet differ in observability (0.313 vs. 0.093). Under held training recipe, architecture configuration determines observability. Across recipes, configuration and training dynamics interact, producing different collapse points. No tested configuration collapses universally across recipes. Observability is determined upstream by the architecture-recipe choice.

Statistical tests. The headline comparison is the matched-scale 3B pair: QWEN 2.5 3B and LLAMA 3B per-probe-seed distributions do not overlap under identical protocol, evaluation data, and token budget per hidden dimension. A permutation test on model-mean ρ_{partial} from 13 models across 6 families is a sensitivity check on cross-family spread, yielding $F = 15.77$, $p = 0.006$, $\eta^2 = 0.92$ (Monte Carlo, 50,000 samples). Three families contribute a single model; the permutation effect size is descriptive rather than inferential, and the matched-scale pair and the Pythia controlled suite carry the inferential weight. In the mixed-effects model (Equation (6)), family is the dominant predictor (LLAMA coefficient = -0.195 relative to GPT-2 baseline), scale is not ($p = 0.951$). Pythia is the controlled within-recipe suite in Section 4 and is analyzed separately because its controlled training tests a different question. Leave-one-family-out

Table 8: Exclusive error catches (observer finds, confidence misses) as a percentage of all errors, across four architecture families at four flag rates. The catch rate increases with ρ_{partial} at low flag rates but converges to 12–15% at 20%, indicating a ceiling set by the error structure rather than by observability.

Model	Family	ρ_{partial}	5%	10%	20%	30%
Mistral 7B	Mistral	0.313	7.3%	11.4%	14.5%	12.6%
GPT-2 124M	GPT-2	0.290	6.6%	10.3%	14.4%	15.9%
QWEN 2.5 7B	Qwen	0.255	6.1%	9.8%	13.0%	12.7%
QWEN 2.5 14B	Qwen	0.214	6.3%	10.4%	13.2%	12.8%
LLAMA 3.2 3B	Llama	0.091	3.8%	8.4%	11.6%	12.0%
LLAMA 3.1 8B	Llama	0.093	5.9%	9.7%	12.0%	11.4%

All values are 3-seed means. Flag rate is the fraction of tokens flagged by each monitor.

sensitivity, Jonckheere-Terpstra within-QWEN 2.5 trend test, supplementary ANCOVA, and the three-level variance decomposition appear in [Section A](#).

Operational catch is bounded by error structure. As a consequence of architecture-dependent observability, activation monitors inherit an upstream ceiling on which errors are catchable. The following rates reflect architectures that preserve the signal; collapsed configurations produce catch rates closer to the random baseline ([Table 8](#)). At 10% flag rate, the observer catches tokens where the model is confident but wrong. For language modeling, an error is a token with loss above the median, so errors occupy half of all tokens. Exclusive catch is the fraction of these errors flagged by the observer but not by confidence.

At 10% flag rate, a wide range in ρ_{partial} across the six models in [Table 8](#) produces a much narrower range in operational catch rate. At 20%, models converge to a 12–15% band, a ceiling set by error structure rather than observability. Exclusive catch has a nonzero random baseline because two rankers with fixed flag rates will disagree by construction. On GPT-2 124M, an analytical random ranker independent of confidence catches 8.1% at 10% and 13.0% at 20%. The observer exceeds random by 2.3 and 1.4 percentage points, with margin narrowing at higher flag rates.

Same 20% ceiling across three downstream tasks. The same 20% ceiling holds across three downstream tasks: SQuAD 2.0 ([Rajpurkar et al., 2018](#)), MedQA-USMLE ([Jin et al., 2021](#)), and TruthfulQA ([Lin et al., 2022](#)), measured on three production instruct models (QWEN 2.5 7B Instruct, Mistral 7B Instruct, Phi-3 Mini Instruct), each using its own WikiText-trained probe applied without task-specific training ([Table 9](#)). SQuAD 2.0 uses the reading-comprehension split with provided context (no retrieval); MedQA-USMLE is four-option multiple choice scored by exact option match; TruthfulQA uses the generation split scored against the reference answer set. Each model generates an answer via greedy decoding with a minimal task prompt. The observer score and max-softmax confidence are averaged over generated tokens (excluding the prompt) to produce per-question scores. Questions are ranked by each score and flagged at the specified rate. A question is an exclusive observer catch if the observer flags it, confidence does not, and the answer is wrong.

Table 9: Exclusive catch rates across three production instruct models and three downstream tasks, using each model’s WikiText-trained probe applied without task-specific training. Columns report catch rate at 10% and 20% flag rate (percentage of errors caught exclusively by the observer). Seven of nine cells at 20% fall between 10.9% and 13.4%; the two exceptions (Phi-3 Mini Instruct on SQuAD at 6.6% and on MedQA at 4.1%) are task-model interactions discussed in [Section 5](#). Confidence has higher single-signal precision at every flag rate; these are the observer’s non-overlapping catches.

Task	QWEN 2.5 7B-I		Mistral 7B-I		Phi-3 Mini-I	
	@10%	@20%	@10%	@20%	@10%	@20%
SQuAD 2.0	5.0%	10.9%	9.7%	11.0%	5.8%	6.6%
MedQA-USMLE	9.4%	13.4%	6.5%	11.2%	1.0%	4.1%
TruthfulQA	7.9%	12.7%	6.7%	10.9%	7.7%	13.1%

Seven of the nine model-task cells at 20% flag rate fall between 10.9% and 13.4%, matching the language-modeling ceiling ([Table 8](#)). Two cells sit below: Phi-3 Mini Instruct on SQuAD (6.6%) and MedQA (4.1%). Phi-3 Mini Instruct preserves observability on WikiText (0.300) and on TruthfulQA (13.1% at 20%), so the SQuAD and MedQA outcomes are task-model interactions rather than a floor on the method. The quality direction learned from Wikipedia next-token

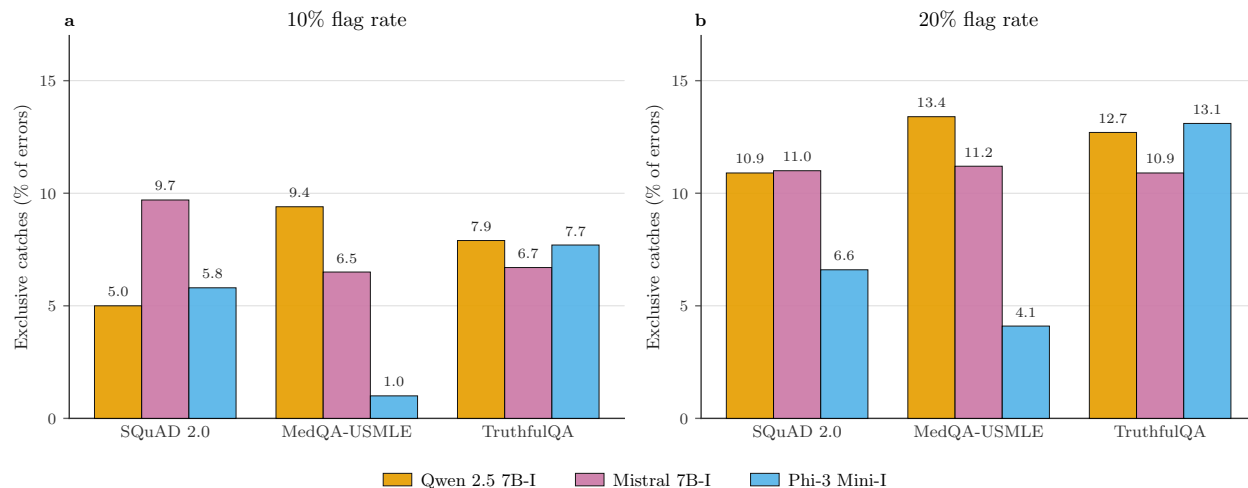


Figure 7: Exclusive catch rates across three tasks and three production instruct models. At 20% flag rate (right), seven of nine cells land in the 10.9–13.4% band, close to the language-modeling ceiling (Table 8). Phi-3 Mini on SQuAD and MedQA are the two exceptions, task-model interactions rather than method floors. All downstream runs use each model’s WikiText-trained probe applied without task-specific training.

prediction reads the same signal across reading comprehension, medical, and factual QA (Figure 7). On MedQA with QWEN 2.5 7B Instruct, among the 40% of questions the model gets wrong, at 20% flag rate roughly one in seven is confidently wrong and caught only by the observer.

TruthfulQA marks the method boundary. The catches above operate over all errors at a fixed flag rate. Among the narrower subset of confidently wrong answers, where the model asserts a fluent falsehood with high confidence, the observer does not discriminate (AUC 0.499 on QWEN 2.5 7B-I, 0.568 on Mistral 7B-I, 0.556 on Phi-3 Mini-I, all near chance). The observer catches token-level prediction failures at the aggregate rate; it does not catch fluent reproduction of learned falsehoods, and the three-model consistency defines that boundary as a property of the method, not of the model.

WikiText-trained probes also transfer to C4 web text (Raffel et al., 2020) (0.155 to 0.192 across four families); training directly on C4 fails on 5 of 7 models tested (Phi-3 Mini and Gemma 3 1B are the exceptions; per-family breakdown in Section D). The probe is portable; the calibration data is not. The observer catches a confidence-invisible error class in every family that preserves the signal. Which families preserve it is the architecture-selection decision this paper surfaces.

6 RELATED WORK

What probes measure. Linear probes were introduced by Alain & Bengio (2017) to monitor intermediate representations. Probing has a known gap between what a probe finds and what the model uses (Belinkov, 2022). Hewitt & Liang (2019) address one side with control tasks: selectivity measures whether a probe finds more than it could from random linguistic labels on the same representation. A probe can pass this test and still be redundant with the model’s own output confidence. Partial correlation with confidence controls reframes the probing-validity question from “more than random?” to “more than the output already provides?” On GPT-2 124M, raw Spearman is 0.549, selective but half confidence-redundant (0.282 after controls). Across 13 models with control-sensitivity data, standard confidence controls absorb $57.7\% \pm 12.6\%$ of the raw probe signal; excluding Gemma 3 1B, 48.6–75.8% (Section 3). For probes targeting decision quality or per-token error, results reported without confidence controls overstate the output-independent component by a comparable factor.

Confidence-independent internal signals. Hidden states encode answer correctness before generation completes (Zhang et al., 2025), and chain-of-thought success is predictable from pre-completion representations (Afzal et al., 2025). Both evaluate discrimination between internal representations and correctness labels without partialling out output confidence, leaving the output-independent component of their reported signals unmeasured. Under our

confidence-controlled protocol, 48.6–75.8% of raw probe signal is absorbed by output confidence across 13 models on analogous next-token quality targets; whether a comparable fraction applies to reasoning and chain-of-thought targets is a question their methodology does not address.

Our scope also extends to variation that fixed-model studies do not surface. The confidence-controlled signal survives on six families and collapses on LLAMA 3B and 8B under the same protocol. Checkpoint dynamics add a further distinction: the quality signal forms in both healthy and collapsed configurations early in training, so the collapse is training-emergent rather than a static property of the converged model. Whether the signals measured by Zhang et al. or Afzal et al. are similarly training-emergent is unknown.

Factuality, hallucination, and deception probes study adjacent activation signals. Han et al. (2025) train lightweight factuality probes on hidden states for long-form generation, achieving competitive hallucination detection with a single forward pass. Their probes target factual accuracy without confidence controls, so the output-independent fraction of their signal is unmeasured. Azaria & Mitchell (2023) train classifiers on activations to detect model-generated falsehoods without confidence controls; whether the detected signal survives partialling out output confidence is untested. Goldowsky-Dill et al. (2025) use linear probes to detect strategic deception from activations, finding high AUROC (0.96–0.999) on evaluation datasets but noting the probe sometimes fires for the topic of deception rather than genuine intent. None of these works test cross-architecture variation or training-emergent collapse.

Verbal uncertainty is a related but distinct representational signal. Ji et al. (2025) find that verbal uncertainty is governed by a single linear feature in representation space, with only moderate correlation to actual semantic uncertainty. The parallel to our single linear direction is limited: their feature controls how confidently the model expresses itself, a style property, while our direction encodes whether the model is actually wrong after removing confidence, a quality property. Verbal assertiveness correlates with output confidence, so their feature may overlap with the component our controls remove. These results suggest that verbal uncertainty and confidence-independent error are represented by distinct components.

Truth directions and contrastive probing. Linear directions for truthfulness have been found via unsupervised consistency (Burns et al., 2023), geometric structure (Marks & Tegmark, 2024), cross-model universality (Bürger et al., 2024), and inference-time causal intervention (Li et al., 2023). These methods target semantic labels and evaluate by discrimination metrics, without isolating the output-independent component via confidence controls. Whether the unsupervised-consistency direction of Burns et al. survives partial correlation with output confidence is an open question; their validation is classification accuracy, not output-independence. Our observer targets per-token loss residuals after removing confidence, so the two lines are complementary. Zou et al. (2023) read linear directions for behavioral concepts from intermediate layers without confidence controls. Our observer targets a different object (confidence-residual per-token loss) and measures a different property (architecture-dependent preservation vs. collapse).

Activation monitoring at scale. Production probes are fragile across distributions (Kramár et al., 2026); Kramár et al. build production-ready activation probes for a model whose representation encodes the relevant signal. This paper identifies the upstream condition: whether the architecture-recipe preserved that signal in the first place. Chain-of-thought monitoring is fragile because training pressures can degrade reasoning legibility (Korbak et al., 2025). Rule-based activation monitoring (Rozenfeld et al., 2026), dynamic safety monitoring (Oldfield et al., 2026), and monitorability metrics (Guan et al., 2025) measure monitoring quality across deployed models without isolating which upstream choices determine signal preservation. This paper identifies that constraint: under controlled training, architecture configuration determines whether a linearly readable signal is preserved.

Calibration and confidence. The 8–12% exclusive error rate is uncovered by calibrated-confidence ranking at the tested flag rates (Guo et al., 2017). Scalar monotone recalibrations of the confidence score preserve Spearman ranks; a nonlinear MLP control on $[\hat{p}_{\max}, \|\mathbf{h}\|]$ absorbs no additional signal ($\rho_{\text{partial}} = 0.289$ vs. 0.282 from the linear control). Nonlinear miscalibration is not the residual’s source. Language models can estimate their own accuracy in some settings (Kadavath et al., 2022), but the output-side predictor on the full representation in the last layer still leaves $r_{\text{OC}} > 0$ at every tested GPT-2 scale.

Semantic uncertainty from hidden states. Kuhn et al. (2023) cluster sampled generations by meaning but require multiple forward passes and still operate on the output distribution. Kossen et al. (2025) approximate semantic entropy from hidden states via linear probes; their probes predict a quantity at the output level (semantic entropy), while ours

measures decision quality after removing confidence. The width-sweep check on our output-side predictor (Section 3) rules out predictor capacity as the explanation.

RAG error detection. Output-level RAG detectors can miss a confidence-invisible error class. NLI faithfulness (Honovich et al., 2022), sample consistency (Manakul et al., 2023), and atomic-claim factual precision (Min et al., 2023) all operate on the generated text. The observer catches a non-overlapping error class: tokens where the model is confident and the output gives no warning but the mid-layer activations encode the failure. On SQuAD 2.0, MedQA-USMLE, and TruthfulQA, a WikiText-trained probe catches 10.9–13.4% of errors exclusively at 20% flag rate in seven of nine model-task cells, matching the language modeling ceiling. Output-level and observer methods are complementary.

Selective prediction and adaptive compute. Output-level abstention leaves an error class uncovered. Early exit (Schuster et al., 2022) and verbalized uncertainty for LLMs (Wen et al., 2025) both make exit decisions based on output-level signals. The observer provides a complementary signal: its value is the non-overlapping catch, not aggregate selective-prediction performance. It flags errors confidence monitoring marks as correct.

Interpretability standards and evasion. Mechanistic interpretability findings require causal methods and separation of correlation from causation (Sharkey et al., 2025). This paper applies cross-domain transfer and target-validity analyses on confidence-controlled probes; mean-ablation results are reported with sign patterns only (magnitudes unreliable under early-layer ablation; Section E). McGuinness et al. (2025) show that models can learn to evade activation monitors. Ji-An et al. (2025) find that LLMs have emergent capacity to monitor and modulate their own activation patterns, a complementary evasion concern. The observer direction is near-orthogonal to dominant variance on GPT-2 124M (PC1 cosine 0.002).

7 DISCUSSION

Architecture determines whether training preserves the signal. Under Pythia’s controlled training, both matched-width configurations form the quality signal at the earliest measured checkpoint, but training erases it in the (24L, 16H) class while the healthy configuration recovers. The static picture is equally sharp: three runs at (24L, 16H) collapse to $\rho_{\text{partial}} \approx 0.10$ despite a $3.5\times$ parameter gap and two Pile variants, while six other configurations sit between 0.21 and 0.38 with no intermediate values (Section 4). At matched 3B scale across families, QWEN 2.5 and LLAMA per-probe-seed distributions do not overlap ($2.9\times$ gap).

Training interacts with configuration across recipes. Under LLAMA’s recipe, observability collapse appears at a different configuration (1B healthy, 3B and 8B collapsed; Section 5). Mistral 7B and LLAMA 3.1 8B share architectural structure yet differ in observability (Section 5), showing the training recipe interacts with configuration. Mean-ablation patching at layer 1 MLP shows opposite signs across the cliff (enhances the observer score in LLAMA 1B, suppresses it in 3B), replicated on Mistral 7B; magnitudes are unreliable under the loss damage, so the sign pattern is the claim (Section A.11).

Mid-layer quality information is not recoverable from the output. Exclusive catches approach 12–15% at 20% flag rate on language modeling, reading comprehension, medical licensing questions, and factual QA (seven of nine model-task cells; two Phi-3 Mini exceptions sit below). On MedQA, the model answers 40% incorrectly; at 20% flag rate, the observer exclusively catches 13.4% of these errors, about one in seven confident-wrong answers that standard monitoring marks as correct. A probe trained on Wikipedia, with no medical data, reads this signal without task-specific training.

Output-independence increases monotonically across the four tested GPT-2 sizes. At 124M, 34% of the quality signal is output-independent. At 1.5B, 60% is. Under a proportional output predictor (MLP bottleneck scaled with hidden dimension), the residual r_{OC} grows from 0.099 at 124M to 0.211 at XL, a $2.1\times$ increase. The absorbed fraction falls from 66% to 32%. On QWEN 2.5 7B, a 512-unit output predictor absorbs no more than a 64-unit bottleneck (Section 3), so the information missing from the output cannot be recovered within tested output-side predictor capacities. The linear observer is the only single-pass method we tested that detects this specific error class (errors invisible to output confidence). Multi-sample approaches such as semantic entropy (Kuhn et al., 2023) and single-pass approximations (Kossen et al., 2025) target an overlapping but distinct error class.

Architecture selection as a monitoring decision. Models that appear comparable under standard capability evaluation may differ substantially in activation monitorability, and the only way to know is to measure. Labs can measure a candidate model’s observability before deployment: a frozen linear probe on mid-layer activations surfaces whether the representation carries the confidence-invisible error signal this monitoring approach can detect. Better monitoring tools cannot recover a signal that training erased from the representation. Nonlinear probes do not cross the healthy floor, no layer preserves the signal in collapsed configurations, output-side predictor capacity is not the bottleneck, r_{OC} collapses to near zero, and the dynamics show training actively erases a signal the architecture initially forms. Once the architecture-recipe choice is made and training completes, the monitoring ceiling is set. No tested probe design recovers healthy-range observability in collapsed configurations. When a candidate architecture collapses, the options are to select a different configuration, to accept reduced monitoring coverage on that error class, or to intervene during training. The dynamics evidence suggests the third path is possible in principle: the signal forms in both configurations, and the erasure occurs during a localizable training window. The naive auxiliary-loss approach fails (see Future Work below), so effective intervention remains an open problem. The largest model tested here is QWEN 2.5 14B. Whether observability persists at frontier scale is unknown, though the QWEN 2.5 0.5B–14B trajectory under one training recipe shows no degradation across a $28\times$ parameter range.

Beyond the architecture dependence, the evidence characterizes these signals more specifically. They occupy a low-variance subspace nearly orthogonal to dominant representation variance, so standard dimensionality reduction and reconstruction-trained decompositions partially obscure them. They are linearly readable but invisible to hand-designed activation statistics. They transfer across text domains, but their training depends on clean calibration data. They are partially discarded by the output layer, and the discarded fraction grows with scale within GPT-2. Confidence controls absorb 57.7% of raw probe signal on average across 13 models. Published probing results targeting decision quality or per-token error that report raw correlations without confidence controls overstate the output-independent component by a factor of two to three. The confidence-controlled protocol is not just a stricter test; it recalibrates how existing probing results should be read.

Limitations and scope. The architecture-dependence claim would be weakened by single-axis controlled training showing smooth interpolation rather than discrete collapse, or by higher-capacity output-side predictors recovering r_{OC} at collapsed configurations. The operational claim would be weakened if confidence-invisible catches disappeared under stronger output-level monitors.

The paper’s claims are tiered by evidence strength. Each tier’s limitations are named here with the experiment that would advance the claim to a stronger tier.

Within-recipe causation. Checkpoint dynamics provide the primary causal evidence: both matched-width configurations form and strengthen the quality signal early in training, but training erases it in the (24L, 16H) class while the (16L, 8H) configuration recovers, at matched final perplexity. The collapse is not architectural incapability but a training-emergent loss. Two limitations are specific to the dynamics evidence. First, the temporal profile is characterized for one matched-dimension pair (1B vs. 1.4B, both $d = 2048$) at 10 checkpoints. The 410M also collapses at (24L, 16H) but was not included in the dynamics analysis because its hidden dimension differs. Second, both configurations dip below the detection floor around step 16,000; why one recovers and the other does not is uncharacterized. Within the Pythia suite, depth and head count co-vary at the (24, 16) class, so this evidence does not isolate which axis drives the preservation failure (depth alone, heads alone, their interaction, or an interaction with training dynamics at this scale). The claim would be weakened if a (24L, 16H) model preserved healthy observability through convergence under modified training hyperparameters. *Advancing the claim: single-axis controlled training at matched scale, and finer-grained checkpoint analysis during the divergence window.*

Observational replication across recipes. Cross-family and LLAMA evidence shows the pattern replicates under different training recipes but does not test cross-recipe causation; the LLAMA distillation provenance is discussed in [Section 5](#). *Advancing the claim: controlled training at matched scale across recipes.*

Operational transfer. Operational utility depends on task-model factors beyond token-level observability and is reported as a separate, scoped claim ([Section 5](#)). Overlap with other single-pass hallucination detectors ([Kuhn et al., 2023](#); [Kossen et al., 2025](#)) on the confidence-invisible subset is untested. *Advancing the claim: direct comparison with semantic-entropy variants on the confidence-invisible subset.*

Method scope. Target residualization is within-distribution; a held-out fit split is untested. Mean-ablation magnitudes are unreliable under early-layer loss damage and are reported as signs only. Adaptive-attack robustness (McGuinness et al., 2025) is untested. *Advancing the claim: clean-corrupted activation patching for mean-ablation; adversarial-evaluation protocols for adaptive attacks.*

Future work. Within-Pythia single-axis controlled training (depth at fixed heads, heads at fixed depth, or their ratio) would isolate whether depth, head count, or their interaction drives observability collapse. Cross-recipe controlled training at matched scale would test whether the collapse configuration is universal or recipe-specific. Separately, deeper analysis of existing checkpoints (finer temporal resolution during the divergence window, layer-profile evolution, the mechanism of the transient 1.4B recovery at step 64,000) could characterize the erasure process without new training runs. Activation patching with clean-corrupted substitution would test whether the layer 1 MLP sign reversal between LLAMA 1B and 3B is a causal pathway or a downstream consequence of earlier representation geometry. A naive auxiliary loss rewarding linear readability of the residualized target at a fixed layer collapses ρ_{partial} on QWEN 2.5 0.5B (from 0.126 under the auxiliary-loss experiment’s lower-budget setup to near zero) while improving perplexity; preserving observability during training is a non-trivial design problem, as the model may route around the auxiliary objective rather than preserving the target direction. Whether training can be modified to preserve a signal the architecture demonstrably represents is an open problem. The dynamics evidence establishes that the signal forms. What training-time conditions determine whether it survives remains open.

8 CONCLUSION

Autoregressive transformers make high-confidence errors, but activation monitoring can catch them only if the model preserves an internal signal that output confidence does not expose. Standard probes substantially overstate this signal: half to two-thirds of what they find in hidden states is output confidence in disguise. After confidence controls, a stable residual remains in some models, and part of that residual is output-independent: it is not recovered by the tested predictors on the final-layer representation.

That residual is not guaranteed. Under Pythia’s controlled training suite, the (24 layers, 16 heads) configuration class undergoes observability collapse across scale and Pile variants, while neighboring configurations preserve a separated healthy signal. The output-controlled residual collapses at the same points, so the lost object is not a probe score but the output-independent, linearly readable information activation monitors need. The signal appears at the earliest measured checkpoint in both matched-width configurations; training preserves it in one architecture and erases it in the other. Cross-family results show the same phenomenon with recipe-dependent collapse maps: QWEN 2.5 and LLAMA differ sharply at matched scale, and Mistral and LLAMA diverge despite similar broad architecture shape.

The observer catches a class of confidence-invisible errors on language modeling, reading comprehension, medical licensing questions, and factual QA without task-specific training. Its value is the complementary error class that confidence marks safe. Confidence has higher single-signal precision. The observer catches what confidence misses.

Architecture selection is a monitoring decision. Whether an activation-based monitor can see a deployed model’s errors depends on the architecture configuration and training recipe chosen upstream. Better monitors cannot recover an error signal that training erased from the representation.

REPRODUCIBILITY AND DISCLOSURE

Reproducibility. This document corresponds to code version v3.3.0, pinned to tag v3.3.0 at <https://github.com/tmcarmichael/nn-observability>. All code, data, and exact model revision hashes are available at that repository. The codebase and results are archived at Zenodo (DOI: 10.5281/zenodo.19805251, version v3.3.0; concept DOI 10.5281/zenodo.19435674). Committed results JSONs are the source of truth; each paper-scope result includes a provenance block recording the model revision, generating script, and timestamp. Results reproduce from a clean clone:

```
git clone https://github.com/tmcarmichael/nn-observability
cd nn-observability && uv sync --extra transformer
just reproduce          # MLP baselines + GPT-2 124M probing
just pythia-suite       # 9 Pythia configurations (GPU)
just downstream-all    # SQuAD, MedQA, TruthfulQA (GPU)
```

Cross-family models (QWEN 2.5, LLAMA, Mistral, Gemma 3, Phi-3) each run via `scripts/run_model.py`; see `scripts/README.md` for per-model commands. Full reproduction requires single-GPU access (H100 or A100). Hugging Face model revisions are pinned in `results/model_revisions.json`. Software: Python 3.12, PyTorch, and Hugging Face Transformers, managed with uv.

LLM disclosure. Claude (Anthropic) assisted with Python scripts for GPU data collection and statistical analysis, experiment notebooks, prose editing, and section-level consistency checks against the results JSONs.

Broader impact. Architecture and training recipe determine whether activation monitoring can catch a deployed model’s confident errors. Monitorability is partially decided at training time, not bolted on later. In high-stakes domains such as medical QA and context-grounded generation, observability is a pre-deployment measurement alongside latency and accuracy. The observer flags a specific class of confidence-invisible failures. It does not detect fluent factual errors, the boundary demonstrated by TruthfulQA, and has not been tested against adaptive attacks. McGuinness et al. (2025) demonstrate that activation monitors can be evaded, and the same threat model applies here: the signal does not ride a dominant variance direction (PC1 cosine 0.002). Deployment should treat activation monitoring as complementary to output-level checks, not as a replacement.

REFERENCES

- Marah Abdin, Jyoti Aneja, Hany Awadalla, et al. Phi-3 technical report: A highly capable language model locally on your phone. *arXiv preprint arXiv:2404.14219*, 2024. URL <https://arxiv.org/abs/2404.14219>.
- Anum Afzal, Florian Matthes, Gal Chechik, and Yftah Ziser. Knowing before saying: LLM representations encode information about chain-of-thought success before completion. In *Findings of ACL*, pp. 12791–12806, 2025. doi: 10.18653/v1/2025.findings-acl.662. URL <https://doi.org/10.18653/v1/2025.findings-acl.662>.
- Guillaume Alain and Yoshua Bengio. Understanding intermediate layers using linear classifier probes. In *International Conference on Learning Representations, Workshop Track*, 2017. URL <https://openreview.net/forum?id=HJ4-rAVt1>.
- Amos Azaria and Tom Mitchell. The internal state of an LLM knows when it’s lying. In *Findings of EMNLP*, pp. 967–976, 2023. doi: 10.18653/v1/2023.findings-emnlp.68. URL <https://doi.org/10.18653/v1/2023.findings-emnlp.68>.
- Yonatan Belinkov. Probing classifiers: Promises, shortcomings, and advances. *Computational Linguistics*, 48(1): 207–219, 2022. doi: 10.1162/coli_a_00422. URL https://doi.org/10.1162/coli_a_00422.
- Stella Biderman, Hailey Schoelkopf, Quentin Gregory Anthony, Herbie Bradley, Kyle O’Brien, Eric Hallahan, Mohammad Aflah Khan, Shivanshu Purohit, USVSN Sai Prashanth, Edward Raff, Aviya Skowron, Lintang Sutawika, and Oskar van der Wal. Pythia: A suite for analyzing large language models across training and scaling. In *International Conference on Machine Learning (ICML)*, volume 202, pp. 2397–2430, 2023. URL <https://proceedings.mlr.press/v202/biderman23a.html>.
- Trenton Bricken, Adly Templeton, Joshua Batson, Brian Chen, Adam Jermyn, Tom Conerly, Nick Turner, Cem Anil, Carson Denison, Amanda Askell, et al. Towards monosemanticity: Decomposing language models with dictionary learning. *Transformer Circuits Thread*, 2023. URL <https://transformer-circuits.pub/2023/monosemantic-features>.
- Lennart Bürger, Fred A. Hamprecht, and Boaz Nadler. Truth is universal: Robust detection of lies in LLMs. In *Advances in Neural Information Processing Systems (NeurIPS)*, 2024. URL <https://openreview.net/forum?id=1Fc2Xa2cDK>.
- Collin Burns, Haotian Ye, Dan Klein, and Jacob Steinhardt. Discovering latent knowledge in language models without supervision. In *International Conference on Learning Representations (ICLR)*, 2023. URL <https://openreview.net/forum?id=ETKGuby0hcs>.

-
- Leo Gao, Stella Biderman, Sid Black, Laurence Golding, Travis Hoppe, Charles Foster, Jason Phang, Horace He, Anish Thite, Noa Nabeshima, Shawn Presser, and Connor Leahy. The Pile: An 800GB dataset of diverse text for language modeling. *arXiv preprint arXiv:2101.00027*, 2021. URL <https://arxiv.org/abs/2101.00027>.
- Gemma Team. Gemma 3 technical report. *arXiv preprint arXiv:2503.19786*, 2025. URL <https://arxiv.org/abs/2503.19786>.
- Aaron Gokaslan and Vanya Cohen. OpenWebText corpus, 2019. URL <https://skylion007.github.io/OpenWebTextCorpus/>.
- Nicholas Goldowsky-Dill, Bilal Chughtai, Stefan Kobi, and Neel Nanda. Detecting strategic deception using linear probes. In *International Conference on Machine Learning (ICML)*, 2025. URL <https://arxiv.org/abs/2502.03407>.
- Aaron Grattafiori, Abhimanyu Dubey, Abhinav Jauhri, et al. The Llama 3 herd of models. *arXiv preprint arXiv:2407.21783*, 2024. URL <https://arxiv.org/abs/2407.21783>.
- Melody Y. Guan, Miles Wang, Micah Carroll, Zehao Dou, Annie Y. Wei, Marcus Williams, Benjamin Arnav, Joost Huizinga, Ian Kivlichan, Mia Glaese, Jakub Pachocki, and Bowen Baker. Monitoring monitorability. *arXiv preprint arXiv:2512.18311*, 2025. URL <https://arxiv.org/abs/2512.18311>.
- Chuan Guo, Geoff Pleiss, Yu Sun, and Kilian Q. Weinberger. On calibration of modern neural networks. In *International Conference on Machine Learning (ICML)*, pp. 1321–1330, 2017. URL <https://proceedings.mlr.press/v70/guo17a.html>.
- Jiatong Han, Neil Band, Muhammed Razzak, Jannik Kossen, Tim G. J. Rudner, and Yarin Gal. Simple factuality probes detect hallucinations in long-form natural language generation. In *Findings of EMNLP*, 2025. URL <https://aclanthology.org/2025.findings-emnlp.880/>.
- John Hewitt and Percy Liang. Designing and interpreting probes with control tasks. In *Proceedings of EMNLP-IJCNLP*, pp. 2733–2743, 2019. doi: 10.18653/v1/D19-1275. URL <https://doi.org/10.18653/v1/D19-1275>.
- Or Honovich, Roei Aharoni, Jonathan Herzig, Hagai Taitelbaum, Doron Kukliansy, Vered Cohen, Thomas Scialom, Idan Szpektor, Avinatan Hassidim, and Yossi Matias. TRUE: Re-evaluating factual consistency evaluation. In *Proceedings of NAACL*, pp. 3905–3920, 2022. doi: 10.18653/v1/2022.naacl-main.287. URL <https://doi.org/10.18653/v1/2022.naacl-main.287>.
- Hamel Husain, Ho-Hsiang Wu, Tiferet Gazit, Miltiadis Allamanis, and Marc Brockschmidt. CodeSearchNet challenge: Evaluating the state of semantic code search. *arXiv preprint arXiv:1909.09436*, 2019. URL <https://arxiv.org/abs/1909.09436>.
- Ziwei Ji, Lei Yu, Yeskendir Koishakenov, Yejin Bang, Anthony Hartshorn, Alan Schelten, Cheng Zhang, Pascale Fung, and Nicola Cancedda. Calibrating verbal uncertainty as a linear feature to reduce hallucinations. In *Proceedings of EMNLP*, pp. 3769–3793, 2025. doi: 10.18653/v1/2025.emnlp-main.187. URL <https://doi.org/10.18653/v1/2025.emnlp-main.187>.
- Li Ji-An, Hua-Dong Xiong, Robert C. Wilson, Marcelo G. Mattar, and Marcus K. Benna. Language models are capable of metacognitive monitoring and control of their internal activations. *arXiv preprint arXiv:2505.13763*, 2025. URL <https://arxiv.org/abs/2505.13763>.
- Albert Q. Jiang, Alexandre Sablayrolles, Arthur Mensch, Chris Bamford, Devendra Singh Chaplot, Diego de las Casas, et al. Mistral 7B. *arXiv preprint arXiv:2310.06825*, 2023. URL <https://arxiv.org/abs/2310.06825>.
- Di Jin, Eileen Pan, Nassim Oufattole, Wei-Hung Weng, Hanyi Fang, and Peter Szolovits. What disease does this patient have? A large-scale open domain question answering dataset from medical exams. *Applied Sciences*, 11(14):6421, 2021. doi: 10.3390/app11146421. URL <https://doi.org/10.3390/app11146421>.
- Saurav Kadavath, Tom Conerly, Amanda Askell, Tom Henighan, Dawn Drain, Ethan Perez, Nicholas Schiefer, Zac Hatfield-Dodds, Nova DasSarma, Eli Tran-Johnson, et al. Language models (mostly) know what they know. *arXiv preprint arXiv:2207.05221*, 2022. URL <https://arxiv.org/abs/2207.05221>.

-
- Tomek Korbak, Mikita Balesni, Elizabeth Barnes, Yoshua Bengio, Joe Benton, Joseph Bloom, et al. Chain of thought monitorability: A new and fragile opportunity for AI safety. *arXiv preprint arXiv:2507.11473*, 2025. URL <https://arxiv.org/abs/2507.11473>.
- Jannik Kossen, Jiatong Han, Muhammed Razzak, Lisa Schut, Shreshth Malik, and Yarin Gal. Semantic entropy probes: Robust and cheap hallucination detection in LLMs. In *International Conference on Learning Representations (ICLR)*, 2025. URL <https://openreview.net/forum?id=YQvvJjLWX0>.
- János Kramár, Joshua Engels, Zheng Wang, Bilal Chughtai, Rohin Shah, Neel Nanda, and Arthur Conmy. Building production-ready probes for Gemini. *arXiv preprint arXiv:2601.11516*, 2026. URL <https://arxiv.org/abs/2601.11516>.
- Lorenz Kuhn, Yarin Gal, and Sebastian Farquhar. Semantic uncertainty: Linguistic invariances for uncertainty estimation in natural language generation. In *International Conference on Learning Representations (ICLR)*, 2023. URL <https://openreview.net/forum?id=VD-AYtP0dve>.
- Kenneth Li, Oam Patel, Fernanda Viégas, Hanspeter Pfister, and Martin Wattenberg. Inference-time intervention: Eliciting truthful answers from a language model. In *Advances in Neural Information Processing Systems (NeurIPS)*, 2023. URL <https://openreview.net/forum?id=aLLuYpn83y>.
- Stephanie Lin, Jacob Hilton, and Owain Evans. TruthfulQA: Measuring how models mimic human falsehoods. In *Proceedings of ACL*, pp. 3214–3252, 2022. doi: 10.18653/v1/2022.acl-long.229. URL <https://doi.org/10.18653/v1/2022.acl-long.229>.
- Potsawee Manakul, Adian Liusie, and Mark J. F. Gales. SelfCheckGPT: Zero-resource black-box hallucination detection for generative large language models. In *Proceedings of EMNLP*, pp. 9004–9017, 2023. doi: 10.18653/v1/2023.emnlp-main.557. URL <https://doi.org/10.18653/v1/2023.emnlp-main.557>.
- Samuel Marks and Max Tegmark. The geometry of truth: Emergent linear structure in large language model representations of True/False datasets. In *Conference on Language Modeling (COLM)*, 2024. URL <https://openreview.net/forum?id=aaajyHYjjsk>.
- Max McGuinness, Alex Serrano, Luke Bailey, and Scott Emmons. Neural chameleons: Language models can learn to hide their thoughts from unseen activation monitors. *arXiv preprint arXiv:2512.11949*, 2025. URL <https://arxiv.org/abs/2512.11949>.
- Stephen Merity, Caiming Xiong, James Bradbury, and Richard Socher. Pointer sentinel mixture models. In *International Conference on Learning Representations (ICLR)*, 2017. URL <https://openreview.net/forum?id=Byj72udxe>.
- Meta. Llama 3.2 3B model card. <https://huggingface.co/meta-llama/Llama-3.2-3B>, 2024. Accessed 2026-04-26.
- Sewon Min, Kalpesh Krishna, Xinxu Lyu, Mike Lewis, Wen-tau Yih, Pang Wei Koh, Mohit Iyyer, Luke Zettlemoyer, and Hannaneh Hajishirzi. FActScore: Fine-grained atomic evaluation of factual precision in long form text generation. In *Proceedings of EMNLP*, pp. 12076–12100, 2023. doi: 10.18653/v1/2023.emnlp-main.741. URL <https://doi.org/10.18653/v1/2023.emnlp-main.741>.
- James Oldfield, Philip Torr, Ioannis Patras, Adel Bibi, and Fazl Barez. Beyond linear probes: Dynamic safety monitoring for language models. In *International Conference on Learning Representations (ICLR)*, 2026. URL <https://openreview.net/forum?id=AGWa8whf92>.
- Alec Radford, Jeffrey Wu, Rewon Child, David Luan, Dario Amodei, and Ilya Sutskever. Language models are unsupervised multitask learners. Technical report, OpenAI, 2019. URL https://cdn.openai.com/better-language-models/language_models_are_unsupervised_multitask_learners.pdf.
- Colin Raffel, Noam Shazeer, Adam Roberts, Katherine Lee, Sharan Narang, Michael Matena, Yanqi Zhou, Wei Li, and Peter J. Liu. Exploring the limits of transfer learning with a unified text-to-text transformer. *Journal of Machine Learning Research*, 21(140):1–67, 2020. URL <https://jmlr.org/papers/v21/20-074.html>.

-
- Pranav Rajpurkar, Robin Jia, and Percy Liang. Know what you don't know: Unanswerable questions for SQuAD. In *Proceedings of ACL*, pp. 784–789, 2018. doi: 10.18653/v1/P18-2124. URL <https://doi.org/10.18653/v1/P18-2124>.
- Shir Rozenfeld, Rahul Pankajakshan, Itay Zloczower, Eyal Lenga, Gilad Gressel, and Yisroel Mirsky. GAVEL: Towards rule-based safety through activation monitoring. In *International Conference on Learning Representations (ICLR)*, 2026. URL <https://openreview.net/forum?id=duntROHZ5R>.
- Tal Schuster, Adam Fisch, Jai Gupta, Mostafa Dehghani, Dara Bahri, Vinh Q. Tran, Yi Tay, and Donald Metzler. Confident adaptive language modeling. In *Advances in Neural Information Processing Systems (NeurIPS)*, 2022. URL <https://openreview.net/forum?id=uLYc4L3C81A>.
- Lee Sharkey, Bilal Chughtai, Joshua Batson, Jack Lindsey, Jeff Wu, et al. Open problems in mechanistic interpretability. *Transactions on Machine Learning Research*, 2025. URL <https://openreview.net/forum?id=91H76m9Z94>.
- Bingbing Wen, Jihan Yao, Shangbin Feng, Chenjun Xu, Yulia Tsvetkov, Bill Howe, and Lucy Lu Wang. Know your limits: A survey of abstention in large language models. *Transactions of the Association for Computational Linguistics (TACL)*, 13:529–556, 2025. doi: 10.1162/tacl_a_00754. URL https://doi.org/10.1162/tacl_a_00754.
- An Yang, Baosong Yang, Beichen Zhang, Binyuan Hui, Bo Zheng, et al. Qwen2.5 technical report. *arXiv preprint arXiv:2412.15115*, 2024. URL <https://arxiv.org/abs/2412.15115>.
- Anqi Zhang, Yulin Chen, Jane Pan, Chen Zhao, Aurojit Panda, Jinyang Li, and He He. Reasoning models know when they're right: Probing hidden states for self-verification. In *Conference on Language Modeling (COLM)*, 2025. URL <https://openreview.net/forum?id=O6I0Av7683>.
- Andy Zou, Long Phan, Sarah Chen, James Campbell, Phillip Guo, Richard Ren, Alexander Pan, Xuwang Yin, Mantas Mazeika, Ann-Kathrin Dombrowski, Shashwat Goel, Nathaniel Li, Michael J. Byun, Zifan Wang, Alex Mallen, Steven Basart, Sanmi Koyejo, Dawn Song, Matt Fredrikson, J. Zico Kolter, and Dan Hendrycks. Representation engineering: A top-down approach to AI transparency. *arXiv preprint arXiv:2310.01405*, 2023. URL <https://arxiv.org/abs/2310.01405>.

APPENDIX

A METHODOLOGY HARDENING

This appendix supplements [Sections 2 and 3](#). Statistical hardening covers 20-seed probe stability, per-family seed variance, and layer-selection and test-split checks. Additional subsections present control-sensitivity analysis, target-validity tests, signal composition via Shapley decomposition, signal geometry, and supplementary statistical tests.

A.1 20-SEED STATISTICAL HARDENING

20 independent observer heads at layer 11 of GPT-2 124M (seeds 42–61): $\rho_{\text{partial}} = 0.282 \pm 0.001$, 95% CI [0.2817, 0.2827], per-seed range [0.279, 0.284], seed agreement 0.993. Layer 11 is the peak layer under the 20-seed hardening protocol; the main 7-seed cross-family protocol peaks at layer 8 with 0.290, consistent with the ± 0.015 top-3 flatness reported in [Section 3](#). This CI covers probe initialization variance on fixed activations and a fixed dataset. It does not capture uncertainty from dataset, checkpoint, or model family variation.

A.2 QWEN 14B SEED DISTRIBUTION

QWEN 2.5 14B has the highest seed variance in the cross-family set ($\tau_{\text{seed}} = 0.851$). Per-seed values cluster near 0.185 (four seeds) or 0.251 (three seeds). The reported mean (0.214) averages across both clusters. The scaling claim ([Section 5](#)) does not depend on the exact value: every seed lands between 0.18 and 0.25, well above the detection threshold and in line with the rest of the Qwen family. The bimodality is preserved under resampling; characterizing the geometric relationship between the two clusters would require per-seed direction data we did not collect.

A.3 LAYER SELECTION AND TEST-SPLIT CONFIRMATION

We select the peak layer using seed 42 and report ρ_{partial} as the mean over seeds 43–49 (or 43–45 for models with fewer seeds) at that fixed layer. Layer profiles are smooth across the top 40–60% of depth. On all models except Gemma 3 1B, the top three candidate layers differ by less than 0.015 in ρ_{partial} : Mistral 7B top-3 range 0.0006, Phi-3 Mini 0.0009, QWEN 2.5 14B 0.0005, QWEN 2.5 3B 0.004, LLAMA 1B 0.004, GPT-2 124M 0.009. Selecting any of the top three layers in place of the reported peak would change no model’s ρ_{partial} by more than 0.015 and no cross-family comparison by more than 0.01.

A separate three-seed test split evaluates the same layer on non-overlapping probe initializations. Across 11 cross-family models with test splits, the mean absolute test-vs-validation gap is 5.2% (max 14.1%; Qwen 1.5B). Eight of 11 models show test < validation; the remaining 3 show test > validation by at most 0.006 absolute. The largest gap (QWEN 2.5 1.5B: 0.236 test vs. 0.275 validation, -14.1%) is consistent with the smaller sample ($n = 3$ vs. $n = 7$): subsampling the validation seeds into groups of three reproduces comparable variance. Cross-family rankings are identical on test data (QWEN 2.5 3B 0.255 vs. LLAMA 3B 0.091, a $2.6\times$ gap), and within-family flatness is preserved (QWEN 2.5 test means span 0.200 to 0.255 across 0.5B–7B).

A.4 CONTROL SENSITIVITY

On GPT-2 124M, raw Spearman of 0.549 drops to 0.283 after softmax-only control, holds at 0.282 after adding norm, and reaches 0.289 under a nonlinear MLP control on $[\hat{p}_{\text{max}}, \|\mathbf{h}\|]$. Softmax is the main confound; norm adds nothing beyond softmax; the residual survives nonlinear deconfounding. Adding logit entropy as a third control absorbs about 31% on top of the standard control (0.196), indicating the observer partially reads the shape of the output distribution, not just the peak.

The control ordering is consistent across architectures. [Table 10](#) extends the GPT-2 124M analysis to a healthy cross-family model (QWEN 2.5 7B base) and to a within-Pythia collapse point (Pythia 410M). In all three, softmax-only and standard (softmax + norm) controls absorb the bulk of the raw signal, norm-only absorbs almost nothing on top, and the nonlinear MLP control yields a similar residual to the linear standard control. The collapse point shows the same control ordering at a shifted absolute scale.

Table 10: Control sensitivity across three architectures. Softmax and standard controls absorb the bulk of the raw signal in all three; norm-only does not remove the residual; nonlinear controls leave similar or slightly higher residuals than standard controls; entropy removes additional output-shape information.

Control	GPT-2 124M	QWEN 2.5 7B base	Pythia 410M (collapse)
None (raw Spearman)	0.549	0.650	0.175
Norm only	0.532	0.646	0.212
Softmax only	0.283	0.236	0.092
Standard (softmax + norm)	0.282	0.240	0.107
Nonlinear MLP	0.289	0.259	0.120
Standard + logit entropy	0.196	0.103	0.035

A.5 VERIFYING “HALF TO TWO-THIRDS IS CONFIDENCE”

The fraction of raw signal absorbed by confidence controls varies across families but is consistently large. Across 13 models in 6 families, standard controls (max softmax + activation norm) absorb $57.7\% \pm 12.6\%$ of the raw Spearman correlation. Excluding Gemma 3 1B (21.1%, anomalous representation geometry), the range is 48.6–75.8% (mean $60.8\% \pm 6.5\%$). The pattern is consistent: confidence is the dominant confound on every architecture tested. The “half to two-thirds” summary in the main text reflects this range.

Absorption gradient tracks observability. Absorbed fraction is not uniform across models but tracks the architecture-dependent observability. Healthy models cluster at 53% to 64% absorbed (Mistral 7B Instruct 53%, Phi-3 Mini 57%, LLAMA 1B 57%, Mistral 7B 58%, QWEN 2.5 3B 56%, QWEN 2.5 0.5B 61%, QWEN 2.5 1.5B 62%, Gemma 3 4B 63%, QWEN 2.5 7B 63%, QWEN 2.5 14B 64%). Collapsed models absorb more: LLAMA 3.2 3B 64% and LLAMA 3.1 8B 76%, the highest in the non-anomalous set: what little raw correlation exists there is almost entirely confidence-redundant. Gemma 3 1B at 21% is the only low-absorption outlier, attributable to the documented representation-geometry artifact (random-probe baseline 0.213). The direction of the gradient, higher absorption where the confidence-independent signal is smaller, is the operational reading of the unified claim: architecture-dependent observability and output-independence are the same property.

A.6 TARGET CIRCULARITY

We construct the binary target by regressing per-token loss on $[\hat{p}_{\max}, \|\mathbf{h}\|]$ via OLS and thresholding the residual at zero. [Section 3](#) presents the complete five-test validity argument; we expand on four of those tests here:

1. Hand-designed readouts of the same activations fail to predict the same target ([Section 3](#)), so the target is not trivially recoverable from activation geometry.
2. The probe succeeds on some architectures (QWEN 2.5 3B 0.263) and fails on others (LLAMA 3B 0.091) under the identical target definition. The variation is in the representations, not the target formula.
3. On QWEN 2.5 7B, within-domain C4 training fails (-0.029 ; LLAMA 8B also fails at -0.062), so the target does not manufacture signal on all activation geometries even within architectures that succeed on WikiText.
4. Seed agreement on the residualized (confidence-removed) observer scores remains 0.991, so the cross-seed consensus is on the confidence-independent component rather than on a shared confidence pathway.

A.7 SIGNAL COMPOSITION (SHAPLEY DECOMPOSITION)

Four named controls account for about 67% of the raw signal under a Shapley value decomposition, computed across all 24 orderings of the 4 controls. The 4-control Shapley total is not directly comparable to the 2-control (max softmax + activation norm) absorption range reported in [Section 3](#) because the control sets differ. The controls are: (i) max softmax confidence, (ii) logit entropy, (iii) geometric typicality (Mahalanobis distance of the activation from the training-set activation mean under the training covariance), and (iv) token frequency (log unigram frequency computed on the probe training corpus). The remaining 33% resists all tested controls. Individual component attributions vary by ordering (confidence ranges from -2% to 26% , entropy from 5% to 36%) because the controls are correlated, but the total

Table 11: GPT-2 scaling curve. Partial correlation is stable across $12\times$ scale. The output-independent component (r_{OC}) grows monotonically; the fraction of signal not captured by the output layer rises from 34% at 124M to 60% at 1.5B. Under a proportional bottleneck (MLP width scaled with hidden dimension), r_{OC} grows further: 0.099 at 124M, 0.102 at 355M, 0.182 at 774M, 0.211 at 1.5B (absorbed fraction falls from 66% to 32%).

Model	Params	Peak layer	ρ_{partial}	\pm std	r_{OC}	$r_{OC}/\rho_{\text{partial}}$	τ_{seed}
GPT-2	124M	L8 (67%)	0.290	0.003	0.099	34%	0.918
GPT-2 Medium	355M	L16 (67%)	0.279	0.006	0.103	37%	0.877
GPT-2 Large	774M	L24 (67%)	0.286	0.009	0.164	58%	0.900
GPT-2 XL	1558M	L34 (71%)	0.290	0.004	0.174	60%	0.952

explained fraction and the unexplained residual are stable. Input-side controls (bigram surprisal) do not absorb the signal.

A.8 SIGNAL GEOMETRY

The observer direction is nearly orthogonal to the dominant variance (PC1 cosine 0.002, top 10 PCs capture 3.7%). The signal reads from the low-variance subspace of the residual stream. Standard dimensionality reduction would miss it, which explains why the SAE probe underperforms raw activations (Section 3): a sparse decomposition optimized for reconstruction concentrates on high-variance directions.

A.9 GPT-2 WITHIN-FAMILY SCALING

Within the GPT-2 family (124M, 355M, 774M, 1.5B), partial correlation is stable across $12\times$ scale (0.279 to 0.290; Table 11). The output-independent component r_{OC} grows monotonically (0.099 \rightarrow 0.174), and the output-independent fraction rises from 34% at 124M to 60% at 1.5B. Scaling preserves total observability but increases the fraction of quality information the output layer discards.

A.10 SUPPLEMENTARY STATISTICAL TESTS

Variance decomposition. A three-level decomposition attributes 88.7% of the variance to family membership, with three singleton-cell families inflating the between-family share by construction; the matched 3B pair (Section 5) and the Pythia controlled suite (Section 4) are the inferential tests.

Uncertainty on η^2 . A bootstrap over model means (10,000 resamples with replacement, $n = 13$) gives a 95% CI of [0.59, 1.00] on η^2 , with the upper bound at the ceiling. The point estimate is close to the maximum because within-family variance is small relative to between-family variance at matched scale; the wide CI reflects the $n = 13$ sample and the singleton-cell structure above, not instability of the measurement.

Leave-one-family-out sensitivity. Removing any single family keeps the permutation test significant ($p \leq 0.023$ in all cases; weakest exclusion: without GPT-2, $p = 0.023$; without Gemma, $p = 0.016$; without Llama, $p = 0.012$). The result is not driven by any single family.

Jonckheere-Terpstra within-QWEN 2.5 trend. A declining trend from 1.5B to 14B is detectable ($p = 0.001$, 74.5% of cross-group comparisons declining). The trend is real but small: the full QWEN 2.5 range (0.214 to 0.275) is less than the QWEN 2.5–LLAMA matched-scale gap. The mixed-effects scale coefficient ($p = 0.951$) confirms within-family variation does not explain cross-family differences.

Supplementary ANCOVA. ANCOVA with scale and family yields family $F(5, 68) = 103.1$, $p = 2.4 \times 10^{-30}$; $\log_{\text{params}} F(1, 68) = 0.04$, $p = 0.85$. Per-seed observations are not independent (shared data and layer selection), so these p -values are anticonservative. The mixed-effects model is the primary test because its random intercepts per model absorb within-model correlation from shared data and layer selection.

Within-Pythia statistical tests. The 8-configuration permutation test (Section 4) is exact: $C(8,2) = 28$ possible 2-vs-6 partitions, and the (24 layers, 16 heads) labeling is the unique partition producing the largest healthy-minus-collapsed gap in ρ_{partial} (0.163), so $p = 0.036$. The healthy mean is 0.269 ($n = 6$, range 0.208 to 0.382); the collapsed mean is 0.106 ($n = 2$, range 0.105 to 0.106). Two supplementary checks: a Mann-Whitney U between the two groups yields $U = 0$,

exact one-sided $p = 0.036$; leave-one-configuration-out across the 8 sizes preserves $\max(\text{collapsed}) < \min(\text{healthy})$ on every removal (minimum surviving gap 0.101, when 2.8B is dropped). Treating 1.4B-deduped as a third replication at the collapse configuration, the 9-point 3-vs-6 exact permutation p-value is 0.012 (1/84); the three replications range from 0.100 to 0.106 (width 0.006) despite $3.5\times$ variation in parameters and two Pile corpora.

Selective prediction. Downstream exclusive catch rates for the observer (WikiText-trained, applied without task-specific training) on SQuAD 2.0, MedQA-USMLE, and TruthfulQA are reported in [Table 9](#). Confidence alone has higher single-signal precision at every tested flag rate; the observer’s value is the non-overlapping catch ([Section 5](#)).

A.11 MECHANISTIC LOCALIZATION OF THE LLAMA CLIFF

Mean-ablation patching on LLAMA 3.2 1B, LLAMA 3.2 3B, and Mistral 7B replaces each component’s output with its dataset mean and measures the change in observer score after partialling out the change in output confidence. Early-layer MLP ablations drive loss up by more than 3.5, indicating the model is substantially damaged; probe scores on these corrupted representations are not effect sizes and are reported as signs only. Activation patching with clean-corrupted substitution would be more reliable.

The directional pattern is consistent. On LLAMA 1B and Mistral 7B (both high-observability), ablating L1 MLP decreases the observer score. On LLAMA 3B (low-observability), the same ablation increases it. The sign reversal at the same component across two scales within one family, with the high-observability direction replicated on a third model from a different family, is consistent with L1 MLP playing different functional roles in high-observability and low-observability models. Whether this reflects a causal role or a downstream consequence of other architectural or training differences requires further investigation. For graded directional ablation on GPT-2 124M, which preserves model function at all intervention strengths, see [Section E](#).

B CHECKPOINT DYNAMICS

[Table 12](#) reports the full checkpoint trajectory for the two matched-width Pythia configurations ($d = 2048$) analyzed in [Section 4](#). Both configurations produce healthy ρ_{partial} and positive r_{OC} at step 256 ($\approx 0.5\text{B}$ tokens). The 1.4B (24L/16H) configuration peaks at step 1,000 ($\rho_{\text{partial}} = 0.314$, $r_{\text{OC}} = 0.113$), then declines. The 1B (16L/8H) configuration follows a similar early trajectory, dips below the detection floor at step 16,000, and recovers by step 32,000. Both configurations converge to comparable perplexity (18–21) at the final checkpoint. Seed agreement tracks ρ_{partial} : it degrades during the mid-training dip and recovers in the 1B but not the 1.4B. Peak layer shifts from late (L12–L18) early in training toward mid-depth (L10–L13) at convergence in the 1B, while the 1.4B returns to late layers (L17) as the signal collapses.

Table 12: Checkpoint dynamics for two matched-width Pythia configurations ($d = 2048$). Both form healthy observability at the earliest measured checkpoint. The (16L/8H) configuration recovers after a mid-training dip; the (24L/16H) configuration does not, converging near the detection floor despite comparable perplexity.

Model	Config	Step	Tokens	Ppl	ρ_{partial}	\pm std	r_{OC}	Peak	τ_{seed}
Pythia 1B	16L/8H	256	537M	1424.9	0.315	0.001	0.079	L12 (75%)	0.979
Pythia 1B	16L/8H	1k	2.1B	139.4	0.303	0.003	0.099	L12 (75%)	0.970
Pythia 1B	16L/8H	2k	4.2B	62.6	0.288	0.001	0.119	L10 (62%)	0.968
Pythia 1B	16L/8H	4k	8.4B	41.0	0.226	0.006	0.097	L8 (50%)	0.951
Pythia 1B	16L/8H	8k	16.8B	32.3	0.242	0.013	0.094	L10 (62%)	0.939
Pythia 1B	16L/8H	16k	33.6B	27.8	0.134	0.008	0.023	L12 (75%)	0.887
Pythia 1B	16L/8H	32k	67.1B	25.1	0.252	0.017	0.122	L10 (62%)	0.932
Pythia 1B	16L/8H	64k	134.2B	22.9	0.257	0.015	0.133	L10 (62%)	0.951
Pythia 1B	16L/8H	128k	268.4B	20.4	0.206	0.012	0.085	L10 (62%)	0.967
Pythia 1B	16L/8H	143k	299.9B	20.6	0.246	0.012	0.120	L10 (62%)	0.974
Pythia 1.4B	24L/16H	256	537M	1660.9	0.297	0.002	0.065	L17 (71%)	0.973
Pythia 1.4B	24L/16H	1k	2.1B	136.3	0.314	0.001	0.113	L18 (75%)	0.977
Pythia 1.4B	24L/16H	2k	4.2B	61.8	0.231	0.002	0.057	L13 (54%)	0.970
Pythia 1.4B	24L/16H	4k	8.4B	40.3	0.254	0.004	0.098	L10 (42%)	0.963
Pythia 1.4B	24L/16H	8k	16.8B	30.4	0.156	0.007	0.037	L11 (46%)	0.940
Pythia 1.4B	24L/16H	16k	33.6B	25.4	0.123	0.008	0.019	L13 (54%)	0.914
Pythia 1.4B	24L/16H	32k	67.1B	22.5	0.113	0.003	0.011	L17 (71%)	0.893
Pythia 1.4B	24L/16H	64k	134.2B	20.6	0.214	0.007	0.092	L13 (54%)	0.942
Pythia 1.4B	24L/16H	128k	268.4B	18.4	0.125	0.004	0.013	L17 (71%)	0.949
Pythia 1.4B	24L/16H	143k	299.9B	18.4	0.106	0.006	0.003	L17 (71%)	0.947

C TOKEN BUDGET SENSITIVITY

Cross-scale comparisons require matching token budgets to hidden dimension. Without this, larger models appear to have weaker signal because their higher-dimensional representations need proportionally more training examples.

At QWEN 2.5 0.5B ($d = 896$), a seven-point sweep from 150 to 1,000 examples per hidden dimension (ex/dim) reveals a detection threshold between 450 and 600 ex/dim (Figure 8). Below 450, ρ_{partial} is flat at 0.145 to 0.153 (7-seed means). At 150 ex/dim the seed std is 0.005, so the measurement is precise; the signal is weak because the probe is under-resourced, not because it is noisy. At 600, ρ_{partial} rises to 0.215, the value reported in Table 6, and continues to 0.232 at 800 and 0.248 at 1,000.

The threshold implies that small models ($d < 1,000$) require more data per dimension than larger models do to produce stable probes. All cross-scale comparisons in this paper use ex/dim ratios above the detection threshold for each model’s hidden dimension. Gemma 3 1B at 150 ex/dim produces a measurable signal (0.388, elevated by the representation-geometry artifact noted in Section 5), consistent with adequate power at this ratio for the d range of models above 0.5B. An earlier measurement of QWEN 2.5 0.5B at 190 ex/dim (0.134) was below the detection threshold. The cross-family table reports the 600 ex/dim result (0.215), which is above the detection threshold and consistent with higher token budgets.

On QWEN 2.5 14B, increasing from 68 to 350 ex/dim on the same model raises ρ_{partial} from 0.194 to 0.214.

The ex/dim metric scales the training set with hidden dimension, so absolute token budgets grow with model size. At the reported ratios, the smallest cross-family model (GPT-2 124M, $d = 768$) uses $\sim 270,000$ training tokens and the largest (QWEN 2.5 14B, $d = 5120$) uses $\sim 1.8\text{M}$. Collapsed models are not bottlenecked by absolute budget: LLAMA 3B (0.091) and 8B (0.093) both run with absolute budgets above 10^6 tokens and still collapse, while Gemma 3 1B reaches 0.388 (geometry-inflated; Section 5) on a much smaller absolute budget. The within-family comparisons (QWEN 2.5 0.5B–14B, LLAMA 1B–8B, Pythia 70M–12B) hold ex/dim above each model’s detection threshold. The threshold’s dependence on absolute budget is out of scope.

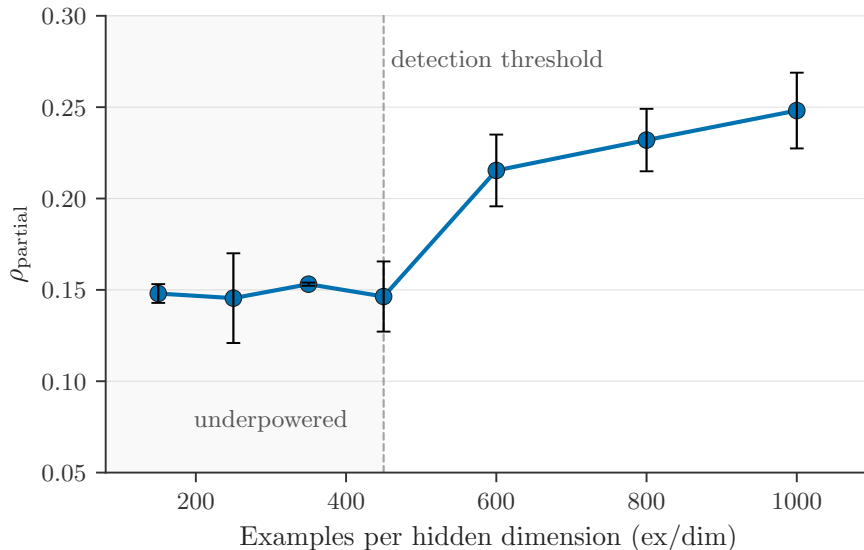


Figure 8: Ex/dim sensitivity at QWEN 2.5 0.5B. Seven token budgets showing ρ_{partial} (7-seed mean) at peak layer. The signal is below the detection threshold between 150 and 450 ex/dim and rises sharply between 450 and 600.

D CROSS-DOMAIN TRANSFER

D.1 THE PROBE IS PORTABLE BUT THE CALIBRATION DATA IS NOT

A WikiText-trained observer transfers to C4 web text across four families (Qwen, Llama, Mistral, Phi), retaining 45–75% of the WikiText signal (Table 13). Gemma 3 1B is excluded from this range; its 114% transfer reflects the representation-geometry anomaly. The probe reads the same quality signal on text it was never trained on.

Table 13: Cross-domain transfer: WikiText-trained probe evaluated on C4 (transfer) vs. probe trained directly on C4 (within-domain). Percentages show C4 transfer as a fraction of WikiText signal. Gemma 3 1B at above 100% is not a generalization improvement: its representation geometry produces a raw Spearman correlation well above the WikiText-residual target threshold on both domains (Section A), so the ratio is driven by an elevated C4 numerator rather than by transfer gain.

Model	WikiText ρ_{partial}	C4 transfer	C4 within-domain
QWEN 2.5 3B	0.263	0.190 (72%)	-0.021
QWEN 2.5 7B	0.255	0.191 (75%)	-0.029
LLAMA 1B	0.286	0.159 (55%)	-0.046
LLAMA 3B	0.091	0.041 (45%)	-0.033
Mistral 7B	0.313	0.155 (50%)	-0.010
Phi-3 Mini	0.300	0.192 (64%)	0.223
Gemma 3 1B	0.388	0.444 (114%)	0.457

The asymmetry is consistent: WikiText→C4 transfer works, but C4→C4 within-domain training fails on 5 of 7 tested models (Phi-3 Mini and Gemma 3 1B are the exceptions; the Gemma result reflects representation-geometry anomaly rather than genuine within-domain training success). The probe is portable across distributions, but training requires calibrated data. C4 is noisier and more heterogeneous than WikiText, so the OLS residualization against confidence produces a noisier binary target. On most families the probe does not converge on a stable direction under these conditions, even with the same total token count.

Gemma 3 1B succeeds on C4 within-domain (0.457), consistent with the representation-geometry anomaly noted in Section 5 (high random baseline 0.213). Phi-3 Mini also succeeds (0.223); we do not have a predictor for which families succeed on within-domain C4 training.

D.2 CODE TRANSFER

On GPT-2 124M, a WikiText-trained probe transfers to CodeSearchNet (Husain et al., 2019) Python at $\rho_{\text{partial}} = 0.539$, exceeding the WikiText source signal (0.290). Transfer to OpenWebText (Gokaslan & Cohen, 2019) is weak (0.086), consistent with the WikiText-to-C4 pattern above. The code result suggests the quality signal encodes structural prediction difficulty (closing brackets, completing function signatures, matching indentation) that generalizes across natural language and code. Code has cleaner syntactic structure than web text, which may explain why the probe finds more signal there than on its training distribution.

D.3 LOW-OBSERVABILITY MODELS

LLAMA 3B shows weak signal on both WikiText (0.091) and C4 transfer (0.041). LLAMA 1B shows the same asymmetry as high-observability models: WikiText 0.286, C4 transfer 0.159, C4 within-domain -0.046 . Low observability at 3B is a property of the model’s representations, not the input domain.

E ABLATION ANALYSIS

E.1 DIRECTIONAL ABLATION

The strongest mechanistic evidence comes from graded directional ablation, which preserves model function at all intervention strengths. The procedure projects out the learned observer direction from the residual stream at layer 8 of GPT-2 124M: $h' = h - \alpha(h \cdot d)d$, where d is unit-normalized. Four controls ground the result: random directions, the confidence direction, a dose-response sweep from 0 to 100%, and bidirectional steering.

Removing the observer direction causes a monotonic loss increase, reaching 0.010 at full (100%) removal. The effect is $2\times$ the random-direction baseline and $57\times$ smaller than the effect of removing the confidence direction. The stronger evidence comes from amplification: adding the direction back reduces loss by -0.013 on observer-flagged tokens versus -0.004 on unflagged tokens, a $3\times$ differential. The amplification effect is direction-specific, sign-specific, and target-specific.

The observer direction is functionally relevant but diagnostic rather than decisive. Destructive removal does not selectively harm flagged tokens; the model’s computation does not depend on this direction the way it depends on confidence.

E.2 MEAN-ABLATION PATCHING

Mean-ablation replaces each component’s output with its dataset mean and measures the change in observer score. On GPT-2 124M, attention at layers 5–7 contributes positively (signal decreases when ablated). The effect is subadditive: ablating layers 5–8 simultaneously produces a smaller effect than the sum of individual ablations, consistent with redundant encoding across multiple attention heads.

Methodological caveat. Mean-ablation of early-layer components causes large loss increases, indicating the model is substantially damaged. Probe scores on corrupted representations measure the probe’s response to pathological inputs, not the component’s contribution to a well-formed signal. All magnitudes from mean-ablation should be interpreted as directional (sign only), not as effect sizes. Activation patching (substituting from a clean run) would provide more reliable attribution.

On QWEN 2.5 7B base:

Component	Sign	Δ_{loss}	Interpretation
Layer 0 attention	+	10.73	ambiguous (model broken)
MLP layer 3	–	6.90	suppresses signal
MLP layer 4	–	7.98	suppresses signal

Table 14: Mean-ablation sign pattern on QWEN 2.5 7B base. MLP layers 3–4 suppress the observer signal (removing them increases the signal).

MLP layers 3–4 suppress the observer signal (Table 14). Layer 0 attention has the opposite sign but the associated loss delta exceeds the usability threshold, so its interpretation is ambiguous under this protocol.

E.3 LAYER FORMATION OF THE OUTPUT-INDEPENDENT COMPONENT

The output-independent component builds from $r_{OC} = 0.065$ (layer 0) to 0.099 (layer 8, 3-seed mean), then drops to 0.077 at the output layer. The signal is constructed during mid-layer computation and partially collapsed into the output distribution by the final layers.